

Article

Entropy Generation and Natural Convection Heat Transfer of (MWCNT/SWCNT) Nanoparticles around Two Spaced Spheres over Inclined Plates: Numerical Study

Huda Alfannakh ¹, Basma Souayah ^{1,2,*}, Najib Hdhiri ², Muneerah Al Nuwairan ³ and Muayad Al-Shaeli ⁴

¹ Department of Physics, College of Science, King Faisal University, P.O. Box 400, Al-Ahsa 31982, Saudi Arabia; halfannakh@kfu.edu.sa

² Laboratory of Fluid Mechanics, Physics Department, Faculty of Sciences of Tunis, University of Tunis El Manar, Tunis 2092, Tunisia; hdhiri_najib@yahoo.fr

³ Department of Mathematics and Statistics, College of Science, King Faisal University, P.O. Box 400, Al-Ahsa 31982, Saudi Arabia; msalnuwairan@kfu.edu.sa

⁴ Institute for Micro-Process Engineering (IMVT), Karlsruhe Institute of Technology, Hermann-von-Helmholtz-Platz 1, 76344 Eggenstein-Leopoldshafen, Germany; muayad.al-shaeli@partner.kit.edu

* Correspondence: bsouayah@kfu.edu.sa or basma.souayah@gmail.com

Abstract: A numerical study is conducted to evaluate the steady natural convective heat transfer problem and entropy generation of both single wall (SWCNT) and multi wall (MWCNT) nanoparticles with water as a base liquid over two spaced spheres. The isothermally heated spheres are located between two plates of short length. The cooled plates are maintained at different inclination angles. A numerical approach based on the finite volume method and multigrid acceleration was used to solve the governing equations. The effects of nanoparticle type, volume fraction, the inclination angle of the plates and the Rayleigh numbers are well-considered. Results reveal that there is a remarkable enhancement of the average Nusselt number over the plates for MWCNT nanoparticles with 63.15% from the inclination angle 0° to 30°. Furthermore, optimal heat transfer rates over the plates for MWCNT nanoparticles equates to 1.9, which is obtained for the inclination 30° and a Rayleigh number of 10⁶. However, for SWCNT nanoparticles, the same equates 0.9, which is obtained for the inclination 90° and a Rayleigh number of 10⁶. The comprehensive analysis is presented under some well-defined assumptions which show the reliability of the present investigation.

Keywords: numerical analysis; heat transfer; MWCNT; SWCNT; entropy production; inner spheres; inclination angle; ecological coefficient of performance



Citation: Alfannakh, H.; Souayah, B.; Hdhiri, N.; Al Nuwairan, M.; Al-Shaeli, M. Entropy Generation and Natural Convection Heat Transfer of (MWCNT/SWCNT) Nanoparticles around Two Spaced Spheres over Inclined Plates: Numerical Study. *Energies* **2022**, *15*, 2618. <https://doi.org/10.3390/en15072618>

Academic Editors: Sandip Mazumder and Jose A. Almendros-Ibanez

Received: 4 February 2022

Accepted: 21 March 2022

Published: 3 April 2022

Publisher's Note: MDPI stays neutral with regard to jurisdictional claims in published maps and institutional affiliations.



Copyright: © 2022 by the authors. Licensee MDPI, Basel, Switzerland. This article is an open access article distributed under the terms and conditions of the Creative Commons Attribution (CC BY) license (<https://creativecommons.org/licenses/by/4.0/>).

1. Introduction

Given the importance of heat transfer enhancement in numerous facets of engineering and the development of effective equipment, countless investigations have been performed to improve the natural convective phenomena and heat transfer in nature and engineering [1,2]. Hence, to meet the growing demand for modern technologies, the efficiency of such thermal equipment needs to be improved [3,4]. Earlier in 1995, a new challenging category of heat transfer fluids, called Nanofluids, was discovered by the mathematician and researcher Choi [5]. They are liquid suspensions that contain nanometer-sized particles (metal or metallic oxide), amalgamated into conventional liquids (water, oil, ethylene glycol, etc.) with thermal conductivities higher than those of the base liquids, and with sizes significantly smaller than 100 nm.

Improvement of nanofluids' utilization in the heat transfer area has made conceivable the new developments in microelectronics, transport, metrology, and so forth [6,7]. In their research study, Kumar et al. [8] studied the flow of Maxwell nanofluid incorporating

MWCNT/SWCNT in a stretching sheet by considering the thermal radiation and magnetic dipole effects.

Hybrid nanofluids SWCNT-TiO₂ and MWCNT-CoFe₂O₄ over a rotating disk under the MHD radiative flow conditions were numerically investigated by Hassan et al. [9]. M. Sheikholeslami et al. [10] applied the Lattice Boltzmann method to numerically simulate the magnetohydrodynamics nanofluid in a cubical cavity heated from below. Authors have considered the Koo–Kleinstreuer–Li correlation. The same CFD discretization method has been used by the same author, M. Sheikholeslami et al. [11], in another research work to investigate the water based nanofluid (Al₂O₃-H₂O) of 3D porous cavity by incorporating an isothermal heated spherical body in the existence of Lorentz forces. Benos et al. [12] studied numerically the MHD natural convection in a shallow enclosure repleted with CNT-nanoparticles; the cavity is internally heated by volumetrically heated sources. CNTs in their two types—SWCNTs-H₂O and MWCNTs-H₂O—are also utilized in the research of Naveed et al. [13] to analyze the heat transfer of semi-infinite, curved, and stretchable regions with a thermal jump and a velocity slip. A marginally related publication by Asjad et al. [14] investigated the MHD viscous fluid flow of carboxyl methyl cellulose (CMC) as a base fluid with carbon nanotube nanoparticles along an inclined plate. The effects of heat source, porosity, chemical reaction, and MHD are considered in this study. A vertical channel filled with TiO₂, Al₂O₃, CNT and Cu nanoparticles with dimpled fins at Rayleigh numbers (Ra) between (3.25×10^7) and (1×10^8) has been studied by Gholami et al. [15] by using the finite volume method. MHD free convection flow of nanofluid of Sodium Alginate (SA) on a solid sphere with prescribed wall temperature is studied by Alawali et al. [16] by using the Keller-box method to solve the PDE.

Amin Shahsavari et al. [17] investigated the Free convection heat transfer and entropy generation characteristics of water-Fe₃O₄/CNT hybrid nanofluid in a concentric annulus. Their results showed that the entropy generation is increasing (both frictional and thermal entropy generation rates) by increasing Fe₃O₄ and CNT concentrations at various Rayleigh numbers. In another scientific contribution, the same authors [18] Investigated the influence of nano additive shape on the natural convection and entropy generation inside a rectangle-shaped finned concentric annulus filled with boehmite alumina nanofluid using a two-phase mixture model. One of the interesting results that authors have found is that the frictional entropy generation rate was enhanced using a higher Rayleigh number and a volume fraction.

A brief overview of the various references makes it clear that the type and properties of the nanoparticles used in the synthesis of nanofluids have a direct influence on the flow and thermal properties [19,20]. Furthermore, the choice of physical domain geometry [21,22] and boundary conditions influence both flow and thermal fields likewise [23,24].

Gravity is the principal factor causing natural convection, and it could be more affected in tilted cavities or channels. Therefore, the effect of inclination angle in convective heat transfer cavities was the center of interest by many researchers [25–27]. Souayah et al. [28] investigated numerically the 3D convective heat transfer of a cubical enclosure induced by a centrally located isothermal cylinder at different inclination angles varying from 0° to 90° by using two ranges of Rayleigh numbers to avoid the unsteadiness. Lately, the influence of enclosure geometry on heat transfer and fluid flow has been made by Yildiz et al. [29]. Therefore, the impact of a dome shaped enclosure has been investigated by considering three types of geometry with different dome heights and inclination angles ($0^\circ \leq \theta \leq 90^\circ$). Likewise, Emami et al. [30] used the two-phase mixture model to analyze numerically the natural convection of a water-based nanofluid (water/Cu) in an inclined porous enclosure filled with porous media. The use of nanofluid, heater configuration, porous media, and the co-effect of the cavity's inclination angle on the enhancement of heat transfer has been investigated in detail. Entropy generation and heat transfer of a square cavity filled with nanofluid of water/Al₂O₃ is analyzed by considering different values of inclination angles ($\theta = 0^\circ, 30^\circ, 60^\circ$ and 90°) and the presence of a magnetic field by Mojtaba et al. [31] in their research paper. An experimental contribution by

Samadzadeh et al. [32] was conducted on natural convection and heat transfer of different nanofluids by considering two enclosures with different dimensions and inclination slopes. Some other important scientific contributions including inclination effects in cavities filled with nanofluids can be found in [33,34].

Frequently in thermal systems, the energy efficiency is a crucial factor. For this reason, researchers are trying to find out how to reduce irreversibility. Research papers mentioning some effective methods to reduce the irreversibility can be found [35–37]. The flow of nanofluids as well as carrier liquids over a spherical body is a motive of interest [38,39]. The analysis of such flows and flows over a spherical geometry cannot be ignored due to multifarious uses in engineering, daily life, and industrial fields such as the fiber, paper, and electronics industries. While considering the applications of the flow over a spherical shaped geometry, academics have attempted to discover the flow with different flow conditions. Chen and Lee [40] investigated the effects of inserted sphere on heat transfer and thermal field of face-centered cubic structure pebble bed. Three horizontal spheres in an equilateral triangular cluster filled with air has been studied by Liu et al. [41] to numerically evaluate the convective heat transfer in this geometry.

By comparing the average Nusselt number of the current geometry with that of a single sphere, it has been found that heat transfer enhances from 64.69% (for the arrangement) to 92.45% (for the single sphere). Bouaziz et al. [42] carried out a numerical study to investigate the mass and heat transfer around a porous sphere saturated with one and two pure liquid components evaporated in a natural convection flow. A marginally related interesting contribution was also done by Souayeh et al. [43] by considering the natural convection phenomena and entropy production of spheres arranged horizontally in a channel with different types of nanoparticles.

To uncover the previously mentioned impacts under the portrayed conditions, the figured outcomes for two inner spaced spheres over two plates filled with MWCNT and SWCNT water-based nanoparticles were analyzed in detail, the plates are tilted under different angle inclinations. Thus, different pertinent parameters are considered such as Ra ($10^3 \leq Ra \leq 10^6$), inclination angles ($0^\circ \leq \alpha \leq 90^\circ$) and nanofluid volume fractions ($2\% \leq \varphi \leq 8\%$) in order to examine convection behavior from different perspectives. Furthermore, the coefficient of thermal performance, the entropy production of the system and the effects of nanofluid type are numerically examined. Therefore, since this type of physical problem under the same parameters has not yet been addressed in the literature survey, the authors believe that the current investigation could be a perfect guidance for the related practical engineering applications; some of them are mentioned in the beginning of introduction section.

2. Methodology

2.1. Physical Problem

Figure 1 shows the actual physical problem and its limit condition. Two internal spaced spheres were considered at a consistent and uniform hot temperature T_h . $D = 0.05$ is the diameter of the spheres which were drenched between two short length plates. Upward and downward plate walls temperature were kept at a cold temperature (T_c). $L = 1$ is the distance between the upward and downward plate walls. The internal spheres centers coordinates are (x_{c1}, z_{c1}) and (x_{c2}, z_{c2}) with $0.3 L$ distance separately, while L is the length of the plates. MWCNT and SWCNT particles with different volume fractions were revolving close to the spheres. The thermophysical features of the used nanoparticles and pure water are presented in Table 1. The plates were maintained under different tilt angles α from 0° to 90° with an increment of 15° .

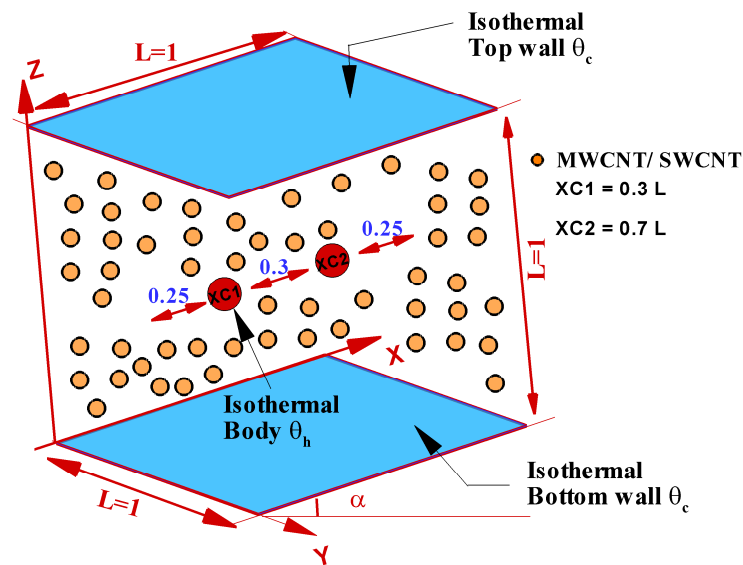


Figure 1. Schematic description of the physical model.

Table 1. Thermophysical properties of pure water and nanoparticles [44].

Property	H ₂ O	MWCNT	SWCNT
ρ (Kg m ⁻³)	997.1	1600	2600
C_p (J Kg ⁻¹ K ⁻¹)	4179	796	425
k (w m ⁻¹ K ⁻¹)	0.613	3000	6600
$\beta \times 10^5$	21	2.8	2.6

2.2. Mathematical Formulation

The current physical problem equations are as follows:

$$\frac{\partial u^*}{\partial x^*} + \frac{\partial v^*}{\partial y^*} + \frac{\partial w^*}{\partial z^*} = 0 \tag{1}$$

$$\rho_{nf} \left(\frac{\partial u^*}{\partial t^*} + u^* \frac{\partial u^*}{\partial x^*} + v^* \frac{\partial u^*}{\partial y^*} + w^* \frac{\partial u^*}{\partial z^*} \right) = -\frac{\partial p^*}{\partial x^*} + \mu_{nf} \left(\frac{\partial^2 u^*}{\partial x^{*2}} + \frac{\partial^2 u^*}{\partial y^{*2}} + \frac{\partial^2 u^*}{\partial z^{*2}} \right) \tag{2}$$

$$\rho_{nf} \left(\frac{\partial v^*}{\partial t^*} + u^* \frac{\partial v^*}{\partial x^*} + v^* \frac{\partial v^*}{\partial y^*} + w^* \frac{\partial v^*}{\partial z^*} \right) = -\frac{\partial p^*}{\partial y^*} + \mu_{nf} \left(\frac{\partial^2 v^*}{\partial x^{*2}} + \frac{\partial^2 v^*}{\partial y^{*2}} + \frac{\partial^2 v^*}{\partial z^{*2}} \right) + \rho_{nf} \beta_{nf} g \cos \alpha (T - T_c) \tag{3}$$

$$\rho_{nf} \left(\frac{\partial w^*}{\partial t^*} + u^* \frac{\partial w^*}{\partial x^*} + v^* \frac{\partial w^*}{\partial y^*} + w^* \frac{\partial w^*}{\partial z^*} \right) = -\frac{\partial p^*}{\partial z^*} + \mu_{nf} \left(\frac{\partial^2 w^*}{\partial x^{*2}} + \frac{\partial^2 w^*}{\partial y^{*2}} + \frac{\partial^2 w^*}{\partial z^{*2}} \right) + \rho_{nf} \beta_{nf} g \sin \alpha (T - T_c) \tag{4}$$

$$\rho_{nf} c_{p,nf} \left(\frac{\partial T}{\partial t^*} + u^* \frac{\partial T}{\partial x^*} + v^* \frac{\partial T}{\partial y^*} + w^* \frac{\partial T}{\partial z^*} \right) = k_{nf} \left(\frac{\partial^2 T}{\partial x^{*2}} + \frac{\partial^2 T}{\partial y^{*2}} + \frac{\partial^2 T}{\partial z^{*2}} \right). \tag{5}$$

To present the governing equations in their dimensionless form, the following dimensionless parameters given below are presented:

$$\tau = \frac{t^*}{t_0}, \quad t_0 = \frac{L^2}{\alpha_f}, \quad P = \frac{P^*}{P_0}, \quad P_0 = \frac{\rho_{nf} \alpha_f^2}{L^2}, \quad u_0 = \frac{\alpha_f}{L}, \quad u = \frac{u^*}{u_0}, \quad v = \frac{v^*}{u_0},$$

$$w = \frac{w^*}{u_0}, \quad \theta = \frac{T - T_c}{T_h - T_c}, \quad x = \frac{x^*}{L}, \quad y = \frac{y^*}{L}, \quad z = \frac{z^*}{L}.$$

Continuity equation:

$$\frac{\partial u}{\partial x} + \frac{\partial v}{\partial y} + \frac{\partial w}{\partial z} = 0. \tag{6}$$

Momentum equations:

$$\frac{\partial u}{\partial \tau} + \frac{\partial(uu)}{\partial x} + \frac{\partial(vu)}{\partial y} + \frac{\partial(wu)}{\partial z} = -\frac{\partial p}{\partial x} + \frac{\mu_{nf}}{\alpha_f \rho_{nf}} \left(\frac{\partial^2 u}{\partial x^2} + \frac{\partial^2 u}{\partial y^2} + \frac{\partial^2 u}{\partial z^2} \right) \quad (7)$$

$$\frac{\partial v}{\partial \tau} + \frac{\partial(uv)}{\partial x} + \frac{\partial(vv)}{\partial y} + \frac{\partial(wv)}{\partial z} = -\frac{\partial p}{\partial y} + \frac{\mu_{nf}}{\alpha_f \rho_{nf}} \left(\frac{\partial^2 v}{\partial x^2} + \frac{\partial^2 v}{\partial y^2} + \frac{\partial^2 v}{\partial z^2} \right) + \frac{(\rho\beta)_{nf}}{\rho_{nf} \beta_f} RaPr\theta \cos \alpha \quad (8)$$

$$\frac{\partial w}{\partial \tau} + \frac{\partial(uw)}{\partial x} + \frac{\partial(vw)}{\partial y} + \frac{\partial(ww)}{\partial z} = -\frac{\partial p}{\partial z} + \frac{\mu_{nf}}{\alpha_f \rho_{nf}} \left(\frac{\partial^2 w}{\partial x^2} + \frac{\partial^2 w}{\partial y^2} + \frac{\partial^2 w}{\partial z^2} \right) + \frac{(\rho\beta)_{nf}}{\rho_{nf} \beta_f} RaPr\theta \sin \alpha \quad (9)$$

Energy Equation:

$$\frac{\partial \theta}{\partial \tau} + \frac{\partial(u\theta)}{\partial x} + \frac{\partial(v\theta)}{\partial y} + \frac{\partial(w\theta)}{\partial z} = \frac{\alpha_{nf}}{\alpha_f} \left(\frac{\partial^2 \theta}{\partial x^2} + \frac{\partial^2 \theta}{\partial y^2} + \frac{\partial^2 \theta}{\partial z^2} \right). \quad (10)$$

Beforehand, the ecological coefficient of thermal performance (ECOP) has been characterized as a model for the assessment of the presentation of expanded surfaces. Here, ECOP is utilized for the assurance of thermal performance pertaining to the current physical model. ECOP depends on the 2nd law of thermodynamics, and it is given by the fraction between heat transfer rates and entropy production. ECOP can be characterized as follows:

$$ECOP = \frac{\overline{Nu}_{Plates}}{S_{tot}}. \quad (11)$$

The boundary conditions used in this study are listed below:

$$\left\{ \begin{array}{l} \bullet \mathbf{u} = \mathbf{w} = \mathbf{v} = 0 \text{ on all walls} \\ \bullet \Theta = 0 \text{ at } [(z = 0, 0 \leq x, y \leq 1) \text{ and } (z = 1, 0 \leq x, y \leq 1)] \\ \bullet \Theta = 1 \text{ on the surface of inner spheres} \end{array} \right.$$

The expressions of Rayleigh (Ra) and Prandtl number (Pr) are as follows:

$$Ra = \frac{g\beta_f(T_h - T_c)L^3}{\alpha_f \nu_f} \text{ and } Pr = \frac{\nu_f}{\alpha_f}.$$

The highly nonlinear and coupled Navier–Stokes with the relevant boundary conditions have been solved numerically based on the finite volume method [45] using a 3D staggered grid. The temporal discretization of the time derivative is performed by a Euler backward second-order implicit scheme. The diffusion terms were advanced implicitly in time, while the nonlinear terms were explicitly advanced. The strong velocity–pressure coupling present in the continuity and the momentum equations is resolved by implementing the projection method [46]. The QUICK scheme of Hayase et al. [47] is implemented to minimize the numerical diffusion for the advective terms according to the momentum equations. The solution of the Poisson equation involves simultaneous iteration on pressure and velocity components to obtain a divergence free velocity field as described by Chorin [48]. For this purpose, accelerated full multigrid methods [49,50] were used to reduce considerably the allowed iterations number. The remaining discretized equations were computed using the red and black point successive over-relaxation method [51] with the choice of optimum relaxation factors. To get the consistent state conditions, the accompanying measure should be fulfilled:

$$\sum_{i,j,k} \left| \chi_{i,j,k}^n - \chi_{i,j,k}^{n-1} \right| \leq 10^{-6}.$$

n is the number of iterations.

A home-made numerical code written in FORTRAN language was utilized for all calculations in the present paper. It is dependent on the finite volume method, projection technique, and multigrid acceleration [52–58].

The local and average Nusselt numbers noted as Nu and \overline{Nu} are defined as follows:

$$Nu = \left. \frac{\partial \theta}{\partial n} \right|_{wall}, \quad \overline{Nu} = \frac{1}{A} \int_0^A Nu dS. \quad (12)$$

n and A are the normal direction and solid spherical body surface area.

2.3. Thermophysical Features of MWCNT and SWCNT Nanoparticles

ρ_{nf} and C_p are representing the effective density and the specific heat capacity respectively, are of the main thermophysical nanofluid features. For suitable calculations of these parameters, the following relations are used:

Nanofluid density [59]

$$\rho_{nf} = \phi \rho_p + (1 - \phi) \rho_f; \quad (13)$$

Specific heat capacity [60]

$$(\rho c_p)_{nf} = (1 - \phi) (\rho c_p)_f + \phi (\rho c_p)_p. \quad (14)$$

The effective thermal conductivity of the nanofluid is approximated by the Maxwell–Garnett [61] model:

$$k_{nf} = \frac{(k_p + 2k_f) - 2\phi(k_f - k_p)}{(k_p + 2k_f) + \phi(k_f - k_p)} k_f. \quad (15)$$

The use of this equation is restricted to spherical nanoparticles where it does not account for other shapes of nanoparticles. This model is found to be appropriate for studying heat transfer enhancement using nanofluids. The viscosity of the nanofluid can be approximated as viscosity of a base fluid containing dilute suspension of fine spherical particles and is given by Brinkman [62]:

Dynamic viscosity [62]

$$\mu_{nf} = \frac{\mu_f}{(1 - \phi)^{2.5}}. \quad (16)$$

Thermal expansion coefficient [63]

$$\beta_{nf} = \left[\frac{\beta_p}{\left(1 + \frac{(1-\phi)\rho_f}{\phi\rho_p}\right)} + \frac{1}{1 + \frac{\phi\rho_p}{(1-\phi)\rho_f}} \right] \beta_f \quad (17)$$

and

$$\alpha_{nf} = \frac{k_{nf}}{(\rho c_p)_{nf}}, \quad (18)$$

knowing that f and p subscripts are referring to the pure fluid and dispersed nanoparticles. The physical properties of MWCNT and SWCNT nanoparticles and the pure water used for this work are listed in Table 1.

2.4. Entropy Production Equations

The entropy generation theory was extensively reported by the researchers [64,65]. The general equation of the entropy generation considered in this problem is given by Equation (19).

$$S_{gen}^* = -\frac{1}{T_0^2} \cdot \vec{q} \cdot \nabla T + \frac{\mu}{T_0} \cdot \Phi^* \quad (19)$$

$$\vec{q} = -k \cdot \text{grad} \vec{T}. \quad (20)$$

The dissipation equation is:

$$\Phi^* = 2 \left[\left(\frac{\partial u^*}{\partial x^*} \right)^2 + \left(\frac{\partial v^*}{\partial y^*} \right)^2 + \left(\frac{\partial w^*}{\partial z^*} \right)^2 \right] + \left(\frac{\partial v^*}{\partial x^*} + \frac{\partial u^*}{\partial y^*} \right)^2 + \left(\frac{\partial w^*}{\partial y^*} + \frac{\partial v^*}{\partial z^*} \right)^2 + \left(\frac{\partial u^*}{\partial z^*} + \frac{\partial w^*}{\partial x^*} \right)^2. \quad (21)$$

The entropy generation is:

$$S_{gen}^* = \frac{k}{T_0^2} \left[\left(\frac{\partial T}{\partial x^*} \right)^2 + \left(\frac{\partial T}{\partial y^*} \right)^2 + \left(\frac{\partial T}{\partial z^*} \right)^2 \right] + 2 \frac{\mu_0}{T_0} \left\{ \left[\left(\frac{\partial u^*}{\partial x^*} \right)^2 + \left(\frac{\partial v^*}{\partial y^*} \right)^2 + \left(\frac{\partial w^*}{\partial z^*} \right)^2 \right] + \left(\frac{\partial v^*}{\partial x^*} + \frac{\partial u^*}{\partial y^*} \right)^2 + \left(\frac{\partial w^*}{\partial y^*} + \frac{\partial v^*}{\partial z^*} \right)^2 + \left(\frac{\partial u^*}{\partial z^*} + \frac{\partial w^*}{\partial x^*} \right)^2 \right\}. \quad (22)$$

After non-dimensionalization, the generated entropy number is given by:

$$N_s = S_{gen}^* \frac{1}{k} \left(\frac{LT_0}{\Delta T} \right)^2, \quad (23)$$

where

$$N_s = \left[\left(\frac{\partial \theta}{\partial x} \right)^2 + \left(\frac{\partial \theta}{\partial y} \right)^2 + \left(\frac{\partial \theta}{\partial z} \right)^2 \right] + \varphi \cdot \left\{ 2 \left[\left(\frac{\partial u}{\partial x} \right)^2 + \left(\frac{\partial v}{\partial y} \right)^2 + \left(\frac{\partial w}{\partial z} \right)^2 \right] + \left(\frac{\partial v}{\partial x} + \frac{\partial u}{\partial y} \right)^2 + \left(\frac{\partial w}{\partial y} + \frac{\partial v}{\partial z} \right)^2 + \left(\frac{\partial u}{\partial z} + \frac{\partial w}{\partial x} \right)^2 \right\}. \quad (24)$$

The total generated entropy is written below and its dimensionless unit

$$S_{tot}^{loc} = \int_0^1 \int_0^1 \int_0^1 N_s dV = \int_0^1 \int_0^1 \int_0^1 (N_{s-TG} + N_{s-VG}) dV = S_{TG}^{loc} + S_{VG}^{loc}. \quad (25)$$

Bejan number, Be , defined as the dimensionless entropy generation due to heat transfer divided by the total entropy generation, is expressed as:

$$Be = \frac{S_{TG}}{S_{TG} + S_{VG}}, \quad (26)$$

where

$$S_T^{loc} = S_{TG}^{loc} + S_{VG}^{loc} \quad (27)$$

$$S_{TG}^{loc} = \left[\left(\frac{\partial \theta}{\partial x} \right)^2 + \left(\frac{\partial \theta}{\partial y} \right)^2 + \left(\frac{\partial \theta}{\partial z} \right)^2 \right] \quad (28)$$

$$S_{VG}^{loc} = \varphi \left[2 \left(\frac{\partial \theta}{\partial x} \right)^2 + 2 \left(\frac{\partial \theta}{\partial y} \right)^2 + 2 \left(\frac{\partial \theta}{\partial z} \right)^2 + 2 \left(\frac{\partial v}{\partial x} + \frac{\partial u}{\partial y} \right)^2 + \left(\frac{\partial w}{\partial y} + \frac{\partial v}{\partial z} \right)^2 + \left(\frac{\partial u}{\partial z} + \frac{\partial w}{\partial x} \right)^2 \right]. \quad (29)$$

With irreversibility coefficient given by:

$$\varphi = \frac{\mu T_0}{k} \left(\frac{u_0}{\Delta T} \right)^2. \quad (30)$$

By Integrating the summation of $S_{TG,loc}$ the local entropy generation or irreversibility due to fluid friction and $S_{VG,loc}$ the local entropy generation or irreversibility due to heat transfer over the domain Ω , we obtain:

$$S_{tot} = \int_{\Omega} S^{loc} d\Omega = \int_{\Omega} S_{TG}^{loc} d\Omega + \int_{\Omega} S_{VG}^{loc} d\Omega = S_{TG} + S_{VG}. \quad (31)$$

3. Grid Testing and Comparison with Previous Numerical Results

3.1. Grid Testing

The sensitivity of the grid was tested for a channel incorporating two horizontal spaced isothermal spheres with base fluid, water ($Pr = 6.2$), revolving between the plates of the plates. The results are computed for a Rayleigh number equating to 10^5 . Different non-uniform grids, $64 \times 64 \times 64$, $80 \times 80 \times 80$, and $96 \times 96 \times 96$, were tested. The results of these calculations are tabulated in Table 2 through the average Nusselt number of the spheres and the plates and the kinetic energy rates. It has been revealed that a grid size of $80 \times 80 \times 80$ (Figure 2) is entirely sufficient to ensure good results.

Table 2. Grid sensitivity analysis.

Grid Size	\overline{Nu}_{sp}	\overline{Nu}_{plates}	Ec_{max}
$48 \times 48 \times 48$	2.3202	0.3895	0.0742
$64 \times 64 \times 64$	2.3072	0.3811	0.0724
Relative Deviation	(0.560%)	(2.156%)	(2.425%)
$80 \times 80 \times 80$	2.3060	0.386	0.071
Relative Deviation	(0.0520%)	(1.269%)	(1.933%)
$96 \times 96 \times 96$	0.3051	0.3641	0.07
Relative Deviation	(0.867%)	(5.673%)	(1.408%)

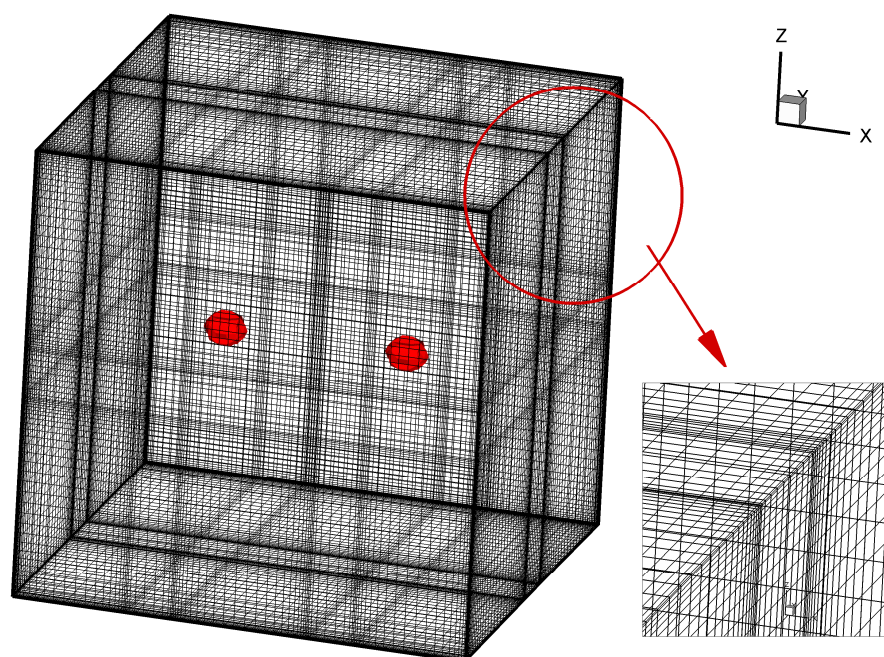


Figure 2. Mesh configuration of the current domain (size $80 \times 80 \times 80$).

3.2. Comparison with Previous Numerical Results

The present numerical solutions were computed and compared with the previous numerical results showed by Yoon et al. [66] and Gulberg and Feldman [67]. The present code results were implemented for the 3D natural convection problem of an isothermal centrally located solid sphere in a cooled outer cuboidal cavity. The values of average Nusselt number for the current calculations along with those found by references [66,67] are shown in Table 3. The values of mean Nusselt number were computed for Ra ranging from 10^3 – 10^6 . As shown in Table 3, the current results of heat transfer values are in well agreement with the previous numerical studies which proves the robustness of the chosen physical configuration.

Table 3. Average heat transfer rates for a cuboidal cavity induced by an isothermal centrally located sphere: Comparison of our numerical results with those found by references [66,67].

Ra	Current Results (Grid Size 80 ³)	Yoon et al. [66]	Gulberg and Feldman [67]
10 ³	6.429	7.575	-----
10 ⁴	7.368	7.859	8.314
10 ⁵	12.093	12.658	13.415
10 ⁶	19.759	20.701	22.344

4. Results and Discussion

Effects of Active Parameters

In the current study, the entropy production and natural convective heat transfer of nanofluids filled two spaced spheres in an inclined arrangement filled with nanofluids of (MWCNT-water and SWCNT-water) are numerically studied using the finite volume method. The different thermo-physical features of the pure water and the chosen nanoparticles are shown in Table 1. The choice of study parameters is performed with carefulness to represent the heat transfer and fluid flow features through graphs and tables. Computations are made for multiple volume fractions ($0\% \leq \phi \leq 8\%$) of nanoparticles, for different ranges of Ra ($10^3 \leq Ra \leq 10^6$) and different inclination angles ($0^\circ \leq \alpha \leq 90^\circ$). The Prandtl number of the pure water is kept constant at 6.2. Figure 3 presents the effects of inclination angle and Rayleigh numbers of MWCNT nanofluid on flow patterns, temperature fields and local entropy maps around the two circular spheres for Ra = 10³ and 10⁵. From this figure, we observe that for a fixed value of Ra (Ra = 10³), streamlines are almost the same while changing the inclination angle from 0° to 60° except a slight change is observed at the angle $\alpha = 90^\circ$. This means that the inclinations angle has no effect on the streamlines for a Ra = 10³. By increasing the value of Ra to 10⁵, the inclination angles have no effect for the angles 0° and 30°. Changes start showing up from $\alpha = 45^\circ$ to 90°; new streamlines appeared at the top right corner of the plates, then they are more developed along the whole top surface of the spheres by increasing α . At $\alpha = 90^\circ$, the developed streamlines form a new cell on the top surface of the inner spheres in a way that we can see two subdivided cells from either side of the spheres. Hence, this can be explained by the fact that in the case of buoyancy-driven flow, the convective fluid motion is monitored by the variation of fluid density. As a matter of fact, at the low value of Ra (i.e., Ra = 10³), the convection current is weak, therefore, the heat transfer in the physical domain is governed mainly by the conduction mode. As the buoyancy force increases (i.e., Ra equates 10⁵), the role of convection in heat transfer become more significant. A similar phenomenon has been observed in the current study while enriching the Ra. The same figure depicts the temperature and entropy maps around the solid spheres, it is to be noted that temperature and entropy contours are almost the same for Ra = 10³ while changing the inclination angle from 0° to 90°. At Ra = 10⁵, obvious changes in temperature and entropy patterns are seen for all the inclination angles.

A general overview of the fluid motion in Figure 4 represents the flow, temperature, and entropy fields for SWCNT nanofluid for different inclination angles of the plates. By considering the angle $\alpha = 0^\circ$ as an exemplary inclination angle, it can be presumed from the contours that streamlines are almost the same for a constant Ra (Ra = 10³) and a variable inclination. However, for Ra = 10⁵ and $\alpha = 30^\circ$, some new contours are showing up at the top left corner of the plates; these contours are expanding on the horizontal surface until they form another group of streamlines on the top region of the spheres.

The temperature and local entropy contours of the spheres in the inclined plates filled with SWCNT nanoparticles for the higher value of Ra (Ra = 10⁵) were examined in the present study, and the results are shown in the same figure (Figure 4). Since the strength of convective motion is increased when increasing the range of Rayleigh number, it is observed that the isotherm shapes and temperature are significantly different in comparison to those

of an Ra equating to 10^3 . However, it is also seen that, remarkably, the contours at $\alpha = 90^\circ$ show a more even circulation. At $\alpha = 0^\circ$, it can be noted that the clockwise circulation is not as regular as at the lower value of Rayleigh number. Alternatively, the fluid circulation is broader and is not well rounded, due to the high strength of flow. For $\alpha = 30^\circ$, an additional smaller circulation is almost recognized at the left upper portion of the plates.

Figure 5 presents the variations of local Nusselt number top (left) and local Nusselt number bottom (right) of MWCNT nanoparticles against Y for different ranges of Ra, volume fraction set to $\varphi = 0.04$ and inclination angle $\alpha = 45^\circ$. We observe that the distributions of the local Nusselt number on the top wall (left) and bottom wall (right) of the plates display an axisymmetric distribution with respect to Y . For the local Nusselt number at the top plate, in the case of Rayleigh number = 10^6 , the maximum of local Nusselt number appears at $Y = 0.85$ with a rate of 3.2. It is also noted that with increasing the Rayleigh number, the local Nusselt number value increases as shown in Figure 5 (left). When $Ra = 10^5$, the maximum of Nusselt number at the top plate is located at $x = 0.8$. Then for $Ra = 10^3$ and 10^4 , the higher rates of local Nusselt numbers are distributed in the wider region and the curves are almost flat so that we cannot define an exact value of the maximum Nusselt number. Furthermore, it is remarked that buoyancy forces increase, and they overcome the viscous forces of MWCNT nanoparticles as heat transfer by convection is dominated, which explains the relatively smaller difference between the Nusselt numbers for the cases of $Ra = 10^3$ and $Ra = 10^4$ compared to the difference between $Ra = 10^5$ and $Ra = 10^6$.

Figure 6 exhibits the variations of local Nusselt number top (left) and bottom (right) of SWCNT nanoparticles against Y for different ranges of Ra, $\varphi = 0.04$ and inclination angle $\alpha = 45^\circ$. As noted in Figure 6, by only changing the nanoparticles type, it is noted that the maximum value of local Nusselt number at the top plate is obtained at $Y = 0.85$ and $Ra = 10^6$ with a rate that equates to 1.5 which is less than half of that compared to MWCNT nanoparticles. However, other constataions are the same, as we note that the increase in the value of local Nusselt number is due to increasing the range of Rayleigh number as revealed in Figure 6 (left). Moreover, an axisymmetric distribution of the local Nusselt number at the bottom and top plates is seen against Y for Figure 6.

Figure 7 demonstrates the effects of varying inclination angle and Ra on the average Nusselt number along with the plates by incorporating both spheres for MWCNT nanoparticles (left) and SWCNT (right) with a volume fraction $\varphi = 4\%$. There is a remarkable improvement in the average Nusselt number of MWCNT particles from the inclination 0° to 30° for Rayleigh numbers equating to 10^6 with 63.15%. In addition, it is clearly observed that there is a marginal difference in heat transfer rates between 0° and 90° inclinations. However, the value of heat transfer surges remarkably by surging the value of Ra and an optimal rate of heat transfer over the plates equating to 1.9 for MWCNT nanoparticles is obtained at ($Ra = 10^6$ and $\alpha = 30^\circ$). Figure 7 (right side) represents the same variations with the same parameters but by considering SWCNT nanoparticles, the average Nusselt number over the cooled plates has a linear profile for the three considered inclination angles. Curves are almost mingled for $\alpha = (0^\circ, 30^\circ, \text{ and } 90^\circ)$ which means inclination angle does not affect the average heat transfer for SWCNT nanoparticle type. The same as in Figure 7 (right side), it is inferred that the average Nusselt number is increasing remarkably by increasing Ra and the optimal heat transfer rate over the plates equating to 0.9 is obtained for ($Ra = 10^6$ and $\alpha = 90^\circ$) for SWCNT nanoparticles.

One more dimensionless parameter is introduced in this study; the Bejan number Be , which represents the fraction of thermal irreversibility to the total irreversibility due to fluid friction and heat transfer effects as explained in Equation (26). Figure 8 (left side) displays the Bejan number profiles of MWCNT nanoparticles ($\varphi = 0.04$) vs. Rayleigh numbers for three inclination angles $\alpha = 0^\circ, 30^\circ$ and 90° . It is obviously seen that the Be number is decreasing monotonously with Ra increment from 10^3 to 10^6 . The inclination angle 90° corresponds to the highest Bejan number followed by the Bejan number of the angle 0° then by the Bejan number corresponding to the angle 30° (the lowest Bejan number). Figure 8 (right side) represents the variations of the Bejan number under the same parameters;

however, the nanoparticle type is changed (SWCNT nanoparticles). We note that the value of $\langle Be \rangle$ increases remarkably by increasing the inclination angle for the Ra ranging from 10^3 to 10^6 . When the Ra is in the range of $10^3 \leq Ra \leq 10^6$, the Be proportionally decreases with Ra, which means that irreversibility due to fluid friction (SVG) is dominant. Eventually, the Bejan number corresponding to MWCNT nanoparticles is less than that of SWCNT nanoparticles.

The dimensionless total entropy generation S_{tot} is the sum of the irreversibility due to a finite temperature gradient and is termed (STG) and the irreversibility due to the effects of fluid friction is termed (SVG), which is found by integrating the local entropy generation rates ($S_{TG;loc}$ and $S_{VG;loc}$) over the domain Ω , as defined in Equation (31). Figure 9 displays the total entropy generation or total irreversibility vs. Ra for inclination angles 0° , 30° and 90° for MWCNT and SWCNT nanoparticles ($\varphi = 0.04$). Therein, the total entropy generation for MWCNT nanoparticles (Figure 9 (right side)) augments with the Rayleigh number for the inclinations 0° and 90° . However, it decreases significantly for the inclination of 30° . Furthermore, it is inferred that $S_{tot}(\alpha = 90^\circ) > S_{tot}(\alpha = 0^\circ) > S_{tot}(\alpha = 30^\circ)$. For the SWCNT nanoparticles (Figure 9 (left side)), the total entropy generation profiles are quite different from those of MWCNT nanoparticles. S_{tot} decreases monotonously between $Ra = 10^3$ and 10^4 for the inclinations of 0° and 30° , then it increases from $Ra = 10^4$ to $Ra = 10^6$. However, for the inclination angle $\alpha = 90^\circ$, the total entropy generation profile follows a piecewise variation, decreasing from $Ra = 10^3$ to 10^4 , increasing from $Ra = 10^4$ to 10^5 then decreasing again from 10^5 to 10^6 . Lastly, we note that $S_{tot}(\alpha = 90^\circ) > S_{tot}(\alpha = 30^\circ) > S_{tot}(\alpha = 0^\circ)$ for SWCNT nanoparticles, which means there is a role change between the inclinations of 0° and 30° in comparison with MWCNT nanoparticles.

To explain the effect of the introduction of MWCNT nanoparticles to the base fluid with a volume fraction ($\varphi = 0.04$) on w -velocity patterns, the projection of the w -velocity vectors is plotted in Figures 10 and 11 subsequently at the inclination angles $\alpha = (0^\circ, 30^\circ, 45^\circ, \text{ and } 90^\circ)$ for $Ra = 10^3$ and 10^5 . For $Ra = 10^3$ and the inclination angle 0° , four clockwise and counterclockwise primary vortices symmetrical to each other are seen to form with a free shear layer in between. For the inclination angle of 30° , the two clockwise vortices of the top right and bottom left corners of the plates are merging to form only one expanded cell along the diagonal. However, the two remaining counterclockwise vortices are seen to be larger in size and stretched. The inclination angle $\alpha = 45^\circ$ has no effect on w -velocity contours compared to $\alpha = 30^\circ$. At $\alpha = 90^\circ$, perfect symmetry is seen against the mid-plane and the core of the vortices is enlarged obviously. It should be noted also that the magnitude of the maximum and minimum w -velocity is increasing with the inclination angle increment; $w_{max} = 0.008$ for $\alpha = 0^\circ$, $w_{max} = 0.021$ for $\alpha = 90^\circ$ and $|w_{min}| = 0.008$ for $\alpha = 0^\circ$, $|w_{min}| = 0.011$ for $\alpha = 90^\circ$.

Figure 11 presents the same velocity contours with the same considered angles of tilt for a higher Rayleigh number set to 10^5 ; it can be noticed that the w -velocity contours become increasingly pronounced with Ra increment and this is due to the rapid movement of the fluid particles in the vicinity of the sphere walls. The results also show that the minus (–) sign of the minimum w -velocity component reflects the flow direction is performed from top to bottom, and the movement of the fluid particles is mostly faster in the vicinity of the sphere walls and not at the side walls of the plates. Overall, the minimum and maximum w -velocity components for $Ra = 10^5$ are much higher than those for $Ra = 10^3$ due to the convective regime domination at a high value of Ra. (i.e., $w_{max} = 0.008$ for $\alpha = 0^\circ$ at $Ra = 10^3$ and $w_{max} = 0.066$ for $\alpha = 0^\circ$ at $Ra = 10^5$).

As it is seen in Figure 12, the average Nusselt number along the plates is plotted against the volume fraction for four ranges of Ra and two types of nanoparticles: MWCNT (solid lines) and SWCNT (dashed lines) for both extreme inclinations $\alpha = 0^\circ$ and 90° . It is inferred that the average Nusselt number along with the plates increases as the Ra increases from 10^3 – 10^6 and it increases as the volume fraction of (SWCNT and MWCNT) nanoparticles increases for only $Ra = 10^3$ and 10^4 . Furthermore, the curves of the corresponding inclinations 0° and 90° are almost confused for $Ra = 10^3$ and 10^4 which means that the

inclination angle does not have an effect on the average heat transfer for small Rayleigh numbers. The inclination angle effect is remarkable for higher Rayleigh numbers 10^5 and 10^6 , where $\overline{Nu}_{plates}(\alpha = 90^\circ) > \overline{Nu}_{plates}(\alpha = 0^\circ)$ for SWCNT and MWCNT. Concerning the variation of the average Nusselt number with nanoparticles volume fraction for Ra (10^5 and 10^6), it is noted that the variation is piecewise (\overline{Nu}_{plates} increases for $2\% \leq \varphi \leq 4\%$ then decreases for $4\% \leq \varphi \leq 6\%$ and increases again for $6\% \leq \varphi \leq 8\%$) and this is for MWCNT nanoparticles. However, the opposite behavior is seen for SWCNT nanoparticles (\overline{Nu}_{plates} increases for $2\% \leq \varphi \leq 6\%$ and decreases for $6\% \leq \varphi \leq 8\%$). It is worth noting that the introduction of nanoparticles leads to this disturbance of variations due to an increase in thermal conductivity and effective dynamic viscosity.

Figure 13 represents the average Nusselt number of the spheres against the volume fraction for four ranges of Ra and two types of nanoparticles: MWCNT (solid lines) and SWCNT (dashed lines) for both extreme inclinations $\alpha = 0^\circ$ and 90° . For $Ra = 10^3$, the curves of the average Nusselt number of the spheres are totally confused for both inclinations which means that augmenting the volume fraction of MWCNT and SWCNT nanoparticles has no effect on average heat transfer at low Rayleigh numbers ($Ra = 10^3$). By increasing the Rayleigh number from 10^4 to 10^6 , the variation of heat transfer curves is obviously seen. Quantitatively speaking, the average heat transfer over the spheres for the inclination 90° and 0° of MWCNT is greater than that corresponding to SWCNT for a volume fraction less than 5%. However, the average heat transfer of SWCNT becomes greater than MWCNT for the inclinations 90° and 0° for a volume fraction greater than 5%. The same constations are revealed in Figure 12. Moreover, the average Nusselt numbers of the spheres are greater than the average Nusselt number of the plates for all ranges of Ra.

Figure 14 presents the profiles of total irreversibility (left side) and the ecological coefficient of thermal performance (right side) against the volume fraction of SWCNT represented by solid lines and MWCNT represented by dashed lines for various Rayleigh numbers and two extreme inclinations, $\alpha = 0^\circ$ and $\alpha = 90^\circ$. It is noted for all Rayleigh numbers that total entropy production augments monotonously with the volume fraction of MWCNT and SWCNT nanoparticles. As shown in Figure 14, the total irreversibility is enhanced with Rayleigh numbers. It is inferred that the overall rate of heat transfer or the irreversibility due to finite temperature gradient increases with φ and Ra, which can be explained by the energy loss due to the irreversibility of the fluid friction effects. It is also shown that total irreversibility curves for $\alpha = 0^\circ$ and 90° are almost confused for all Rayleigh numbers which means that the inclination angle does not affect the total entropy generation. Additionally, Figure 14 shows that the ECOP coefficient is decreasing while the nanoparticles volume fraction is increasing for the complete range of Ra. On the other hand, for both types of nanoparticles, ECOP decreases from 0.82 for $Ra = 10^3$ to 0.24 for $Ra = 10^6$ (70.73% diminution). In addition, ECOP decreases when the nanoparticles volume fraction increases at $Ra = 10^3$ (for only φ varying from 4% to 8%), 10^4 , 10^5 , and 10^6 .

The trajectory of fluid particles for MWCNT nanoparticles at different ranges of Ra (from 10^3 to 10^6) at the inclination angle $\alpha = 0^\circ$ is demonstrated in Figure 15. From this figure, it is inferred that at the lowest value of Rayleigh numbers $=10^3$, the overall structure of the fluid flow is normal. Then, by increasing the range of Rayleigh number (10^4 – 10^6) the fluid particles close to the sphere's region are moving towards the upper region of the plates. Besides, they bend towards the side walls of the plates. It is also worth noting that the velocity of the fluid particles for the inclination angle $\alpha = 0^\circ$ is increasing until they attain their maximum at $Ra = 10^5$ and 10^6 ($|w| = 0.05$), which is five times greater than the fluid particles' speed at $Ra = 10^3$ ($|w| = 0.01$).

For the inclination angle $\alpha = 90^\circ$ and the same nanoparticles type (MWCNT), the behavior of the fluid particles' trajectory is presented in Figure 16. The behavior of fluid particles this time is quite different as it is divided into two rolls located at the top right corner and bottom left corner of the cavity. Furthermore, the fluid particle rolls are becoming more compact for Ra numbers starting from 10^4 to 10^6 due to their strong circulation for high Rayleigh numbers. Quantitatively speaking, for the same $\alpha = 90^\circ$, the velocity of

the fluid particles at $Ra = 10^6$ is ten times higher than those for $Ra = 10^3$; ($|w| = 0.02$ for $Ra = 10^3$ and $|w| = 0.21$ for $Ra = 10^6$). On the other hand, the velocity of the fluid particles for the same $Ra = 10^6$ and the inclination angle $\alpha = 90^\circ$ are four times higher than those for the inclination angle $\alpha = 0^\circ$; ($|w| = 0.02$ for $\alpha = 90^\circ$ and $|w| = 0.05$ for $\alpha = 0^\circ$).

Tables 4–7 summarize the heat transfer rates of MWCNT and SWCNT nanoparticles for the parallel plates and inner spheres subsequently. For the same type of nanoparticles (either MWCNT or SWCNT), it is noted that $\overline{Nu}_{sphere}(MWCNT) > \overline{Nu}_{plates}(MWCNT)$ and $\overline{Nu}_{sphere}(SWCNT) > \overline{Nu}_{plates}(SWCNT)$. It is also inferred that average heat transfer rates are increasing linearly with the nanoparticles volume fraction and the Rayleigh number; however, it is almost constant by increasing the inclination angle of the plates. A comprehensive comparison between MWCNT and SWCNT nanoparticles shows that nanoparticle type has no effect on average Nusselt number values. Furthermore, average Nusselt number values are almost the same for the spheres and the plates.

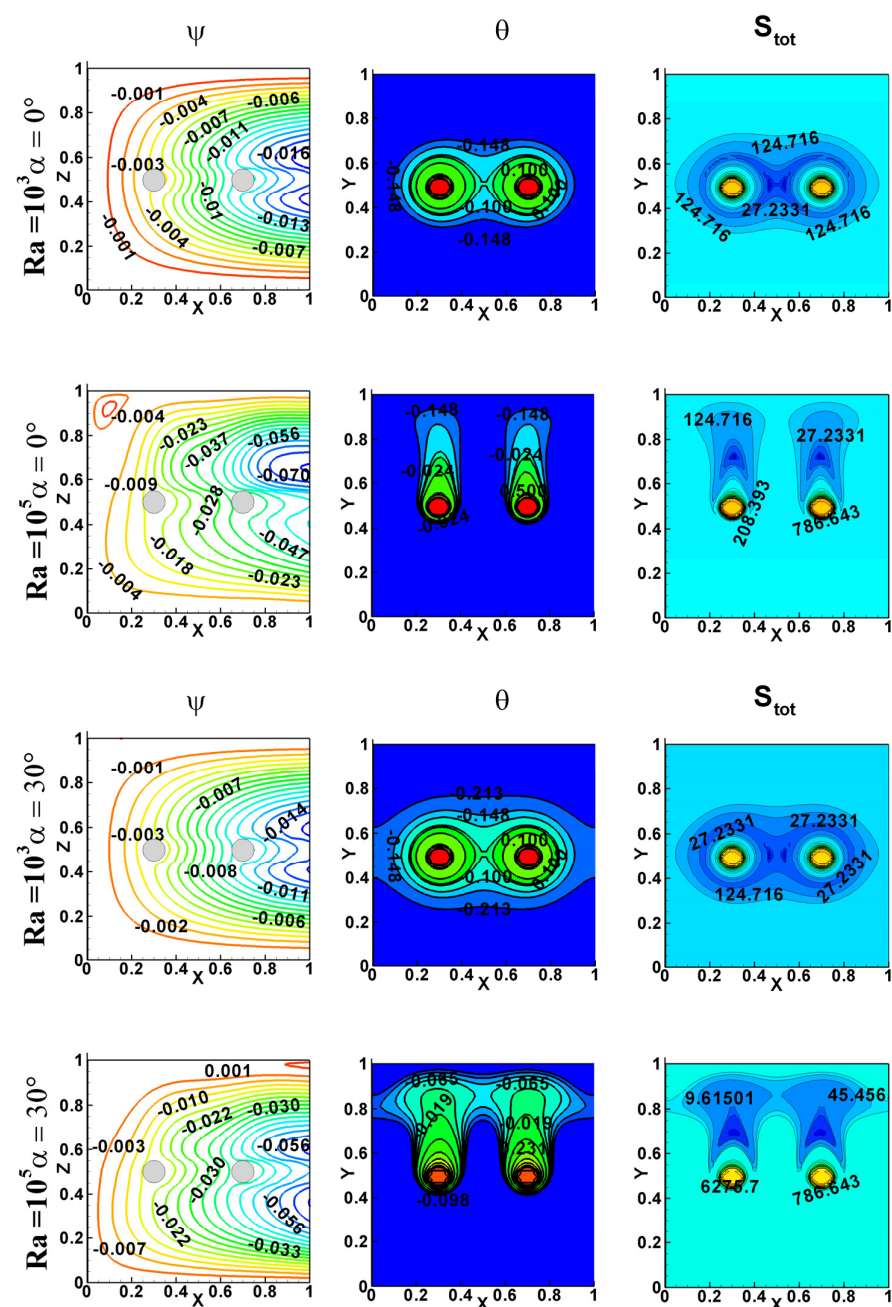


Figure 3. Cont.

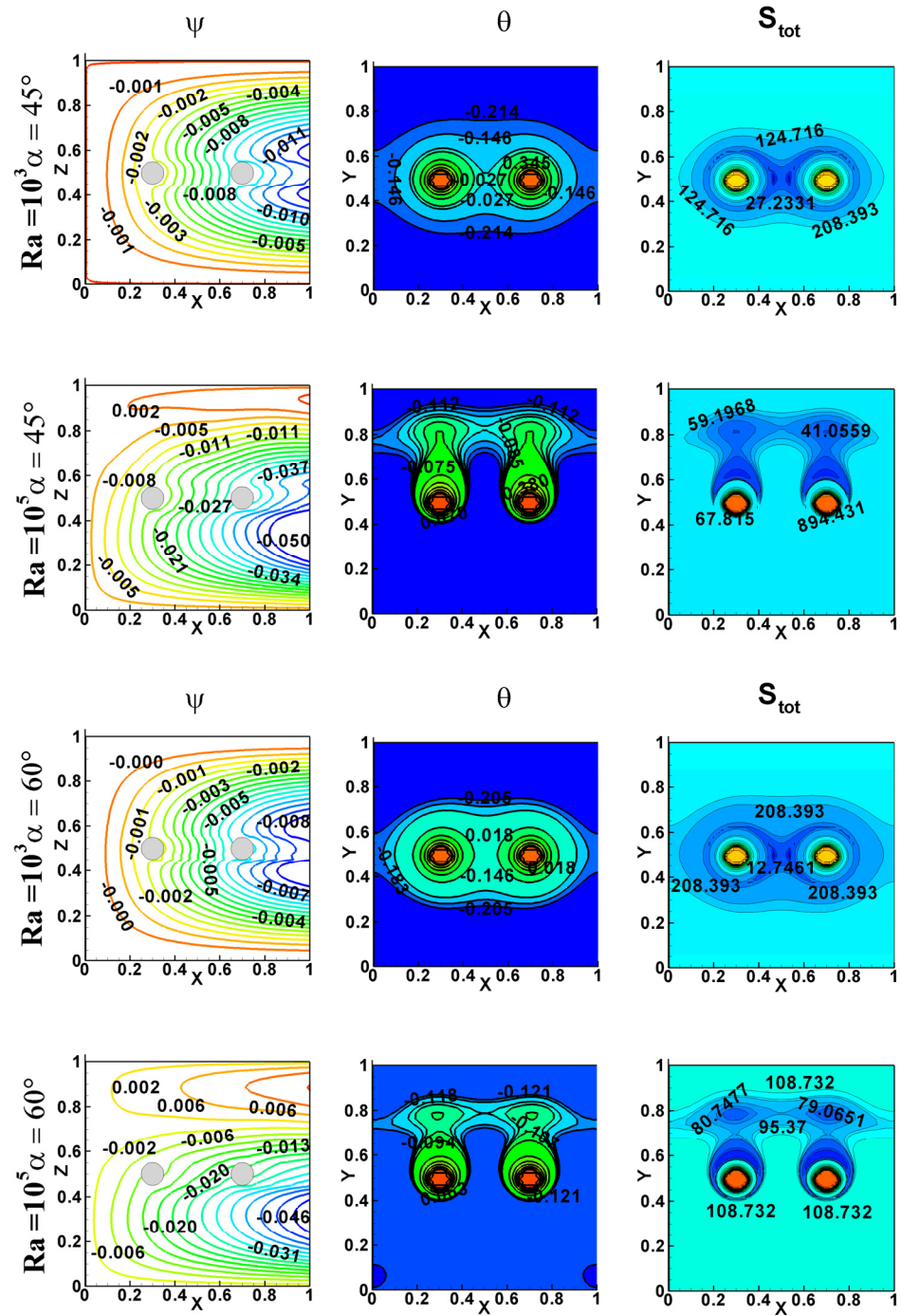


Figure 3. Cont.

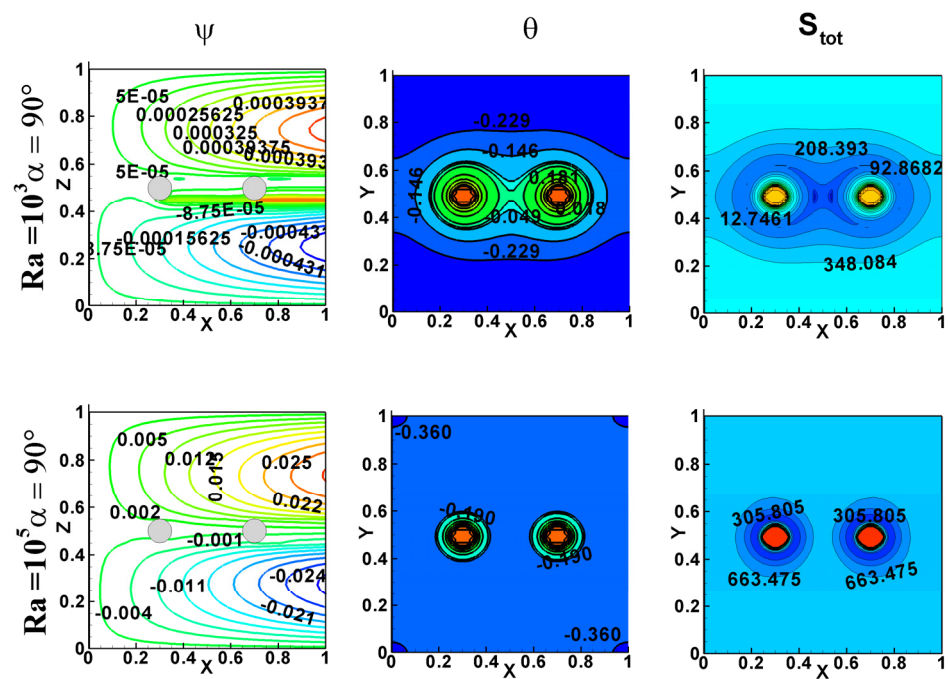


Figure 3. Flow field at (x, z) plane, temperature field at (x, y) plane and local entropy field at (x, y) plane of MWCNT nanoparticles at $Ra = 10^3$ and 10^5 , $\alpha = (0^\circ, 30^\circ, 45^\circ, 60^\circ$ and $90^\circ)$, $\varphi = 0.04$.

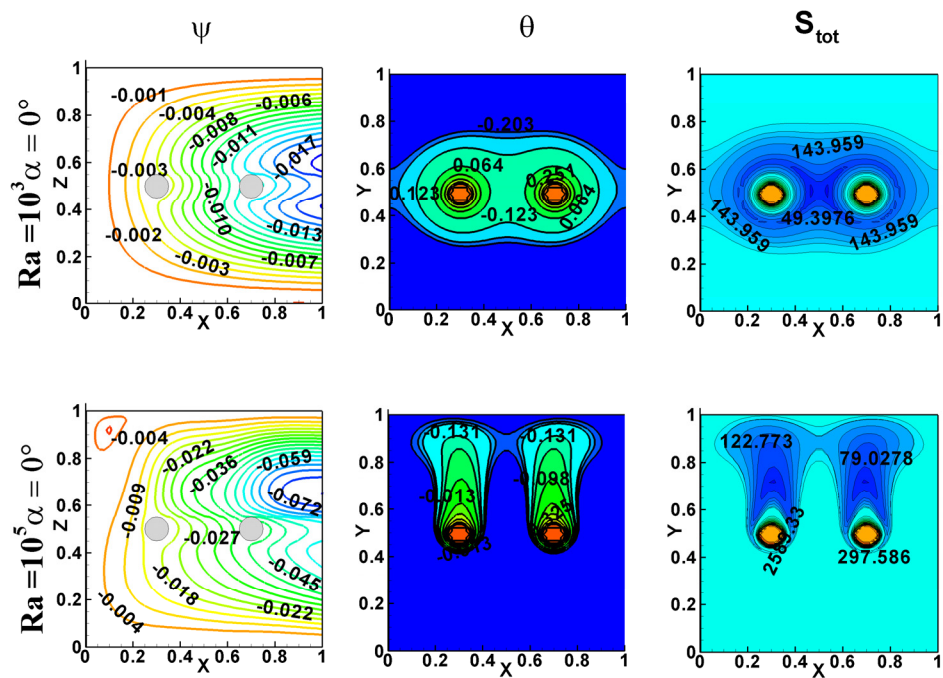


Figure 4. Cont.

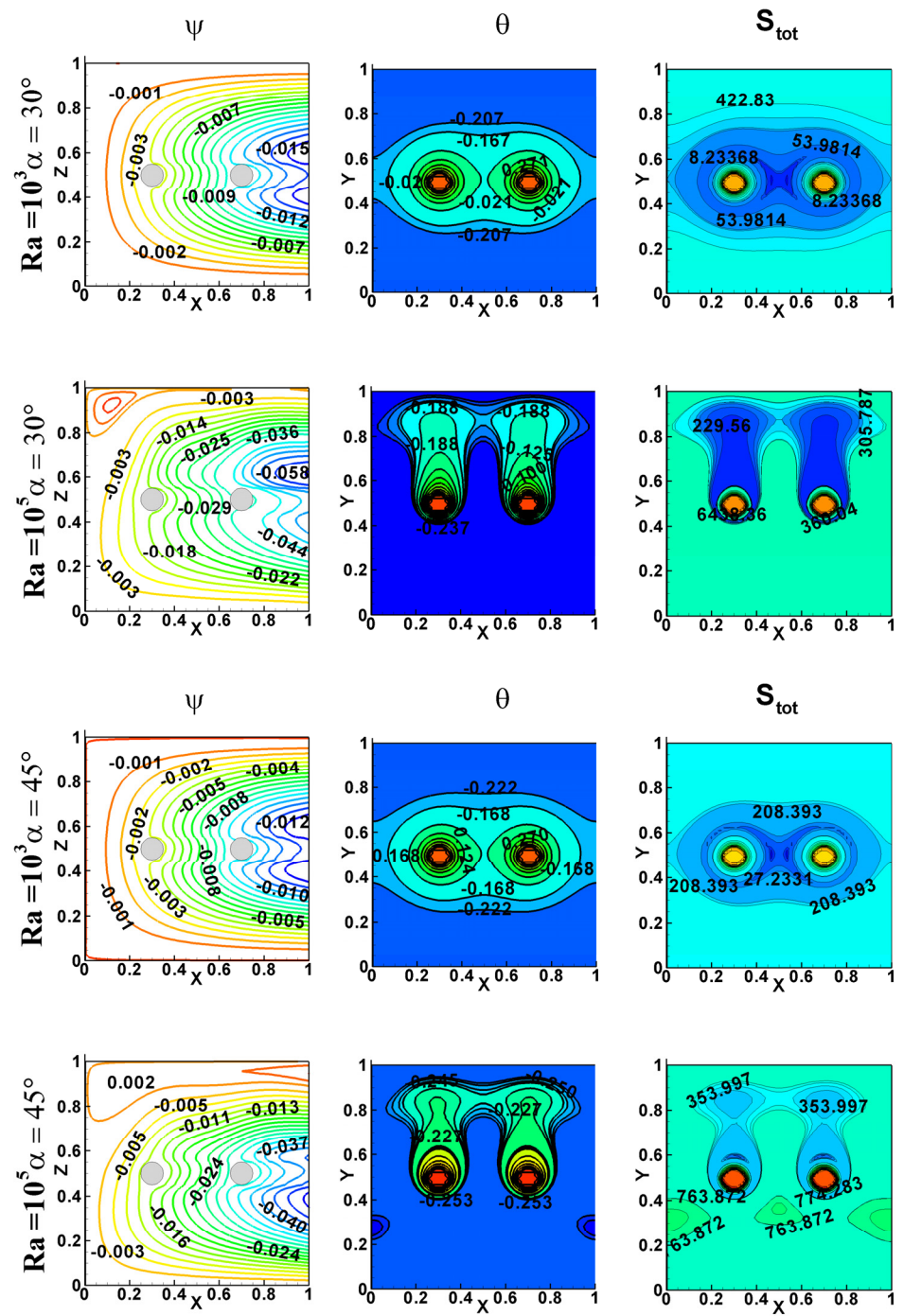


Figure 4. Cont.

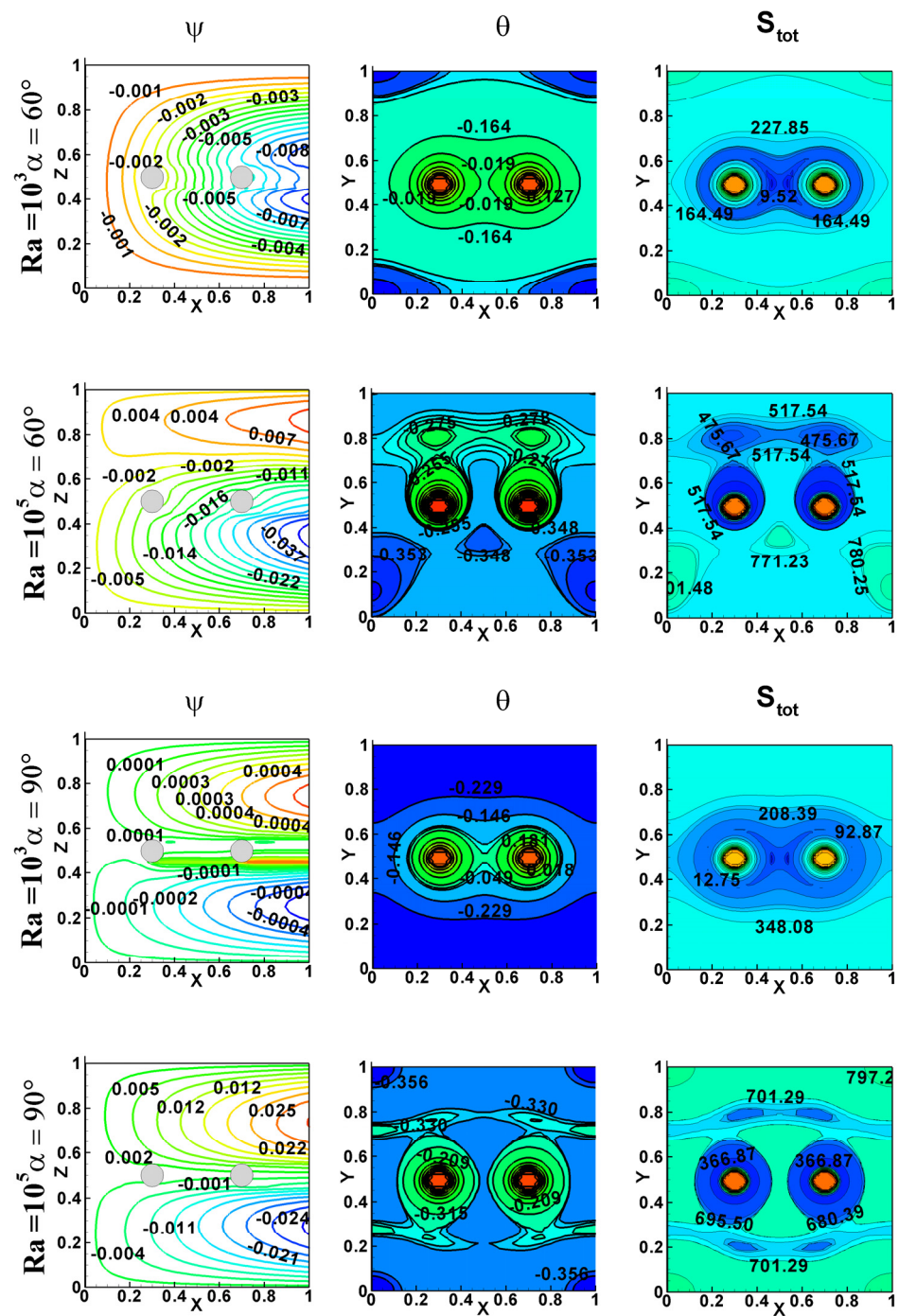


Figure 4. Flow field at (x, z) plane, temperature field at (x, y) plane and local entropy field at (x, y) plane of SWCNT nanoparticles at $Ra = 10^3$ and 10^5 , $\alpha = (0^\circ, 30^\circ, 45^\circ, 60^\circ$ and $90^\circ)$, $\phi = 0.04$.

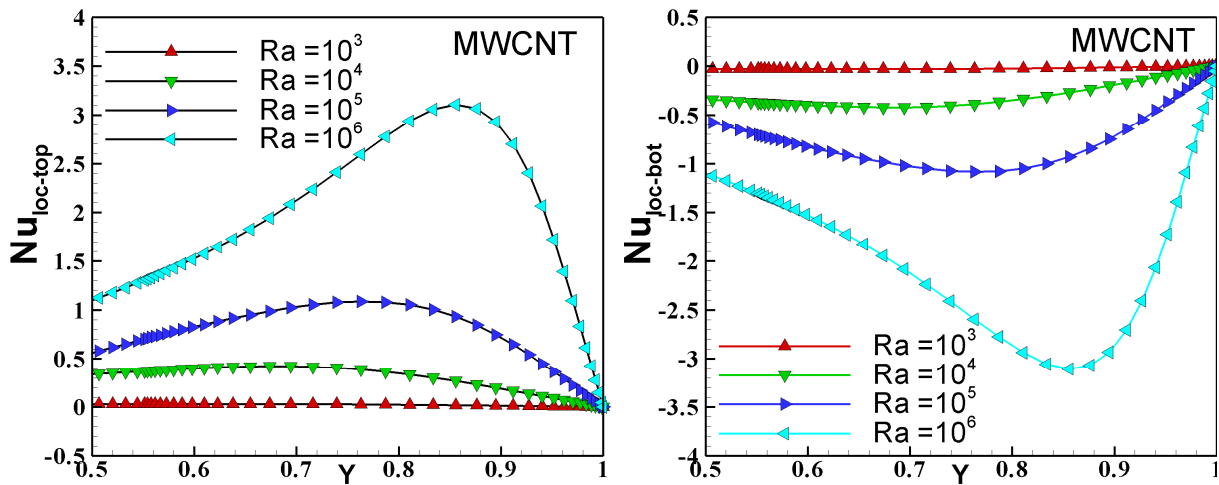


Figure 5. Variation of the local Nusselt number with Y on the top (left) and bottom hand-side wall (right) for MWCNT nanoparticles at different Ra , $\phi = 0.04$ and $\alpha = 45^\circ$.

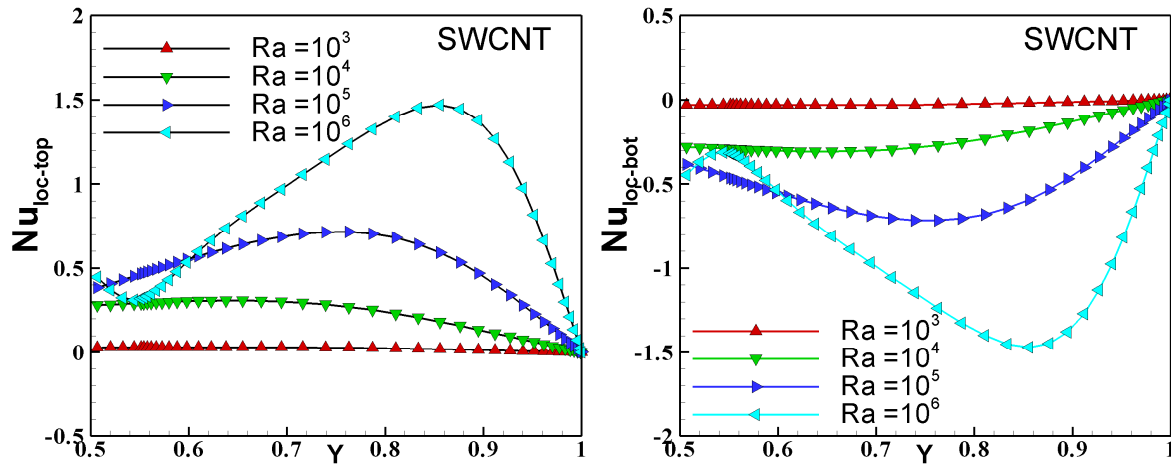


Figure 6. Variation of the local Nusselt number with Y on the top (left) and bottom-hand side wall (right) for SWCNT nanoparticles at different Ra , $\phi = 0.04$ and $\alpha = 45^\circ$.

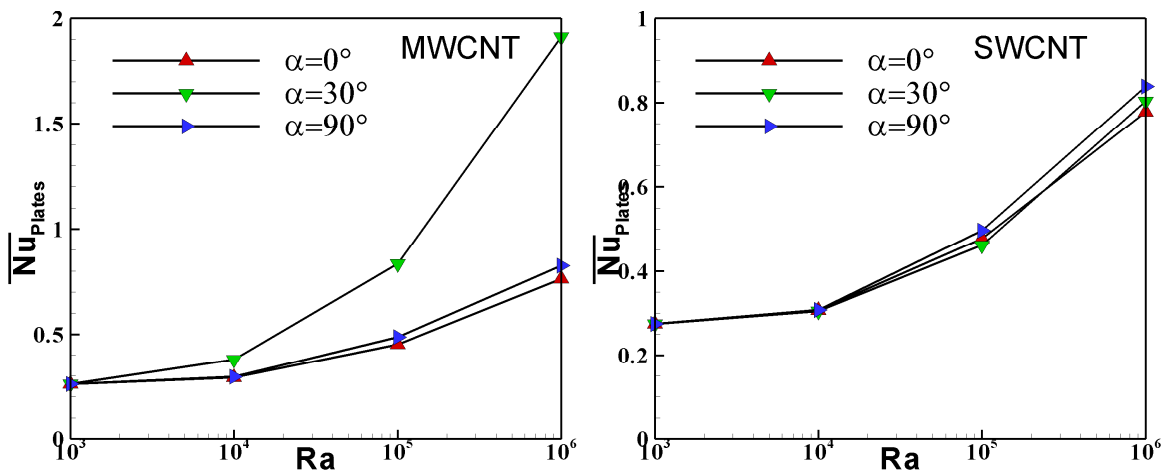


Figure 7. Average Nusselt number profiles over the plates of MWCNT (left) and SWCNT (right) nanoparticles against Rayleigh numbers for different values of inclination angles $\alpha = (0^\circ, 30^\circ$ and $90^\circ)$, $\phi = 0.04$.

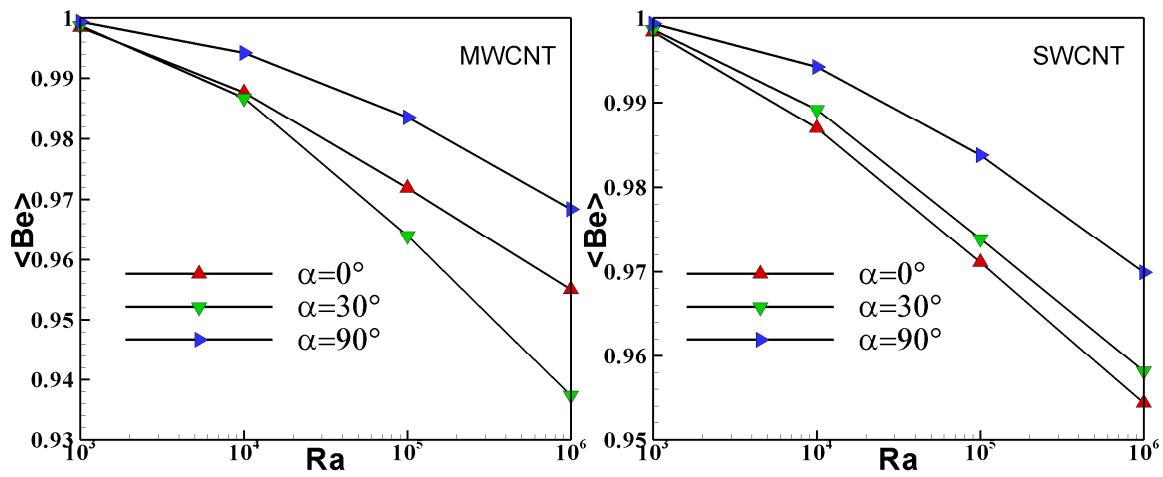


Figure 8. Variation of Bejan number profiles of MWCNT (left) and SWCNT (right) nanoparticles against Rayleigh numbers vs. Rayleigh numbers for different values of inclination angles $\alpha = (0^\circ, 30^\circ$ and $90^\circ)$, $\phi = 0.04$.

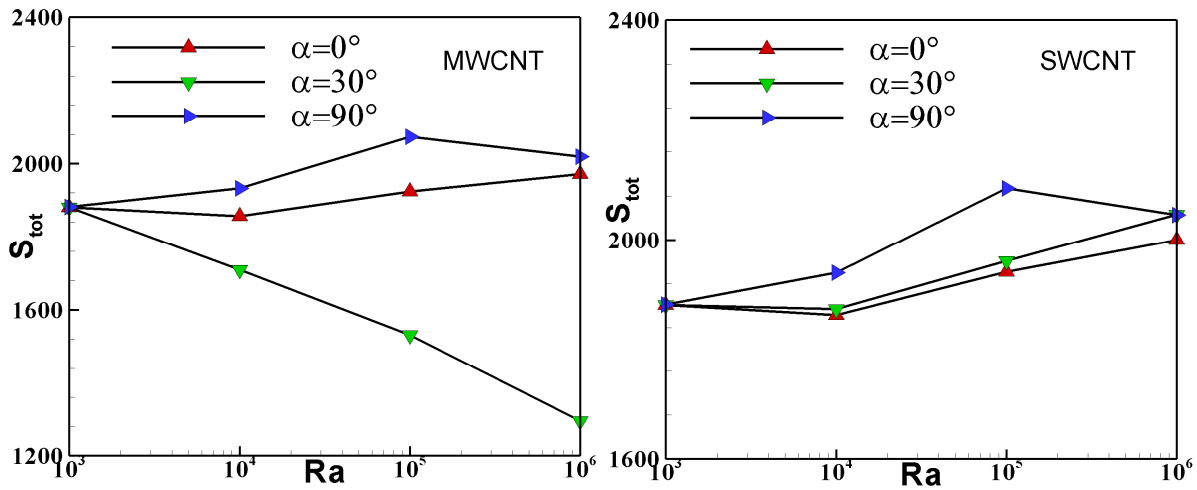


Figure 9. Total entropy generation or total irreversibility profiles of MWCNT (left) and SWCNT (right) nanoparticles against Rayleigh numbers against Rayleigh numbers for different values of inclination angles $\alpha = (0^\circ, 30^\circ$ and $90^\circ)$, $\phi = 0.04$.

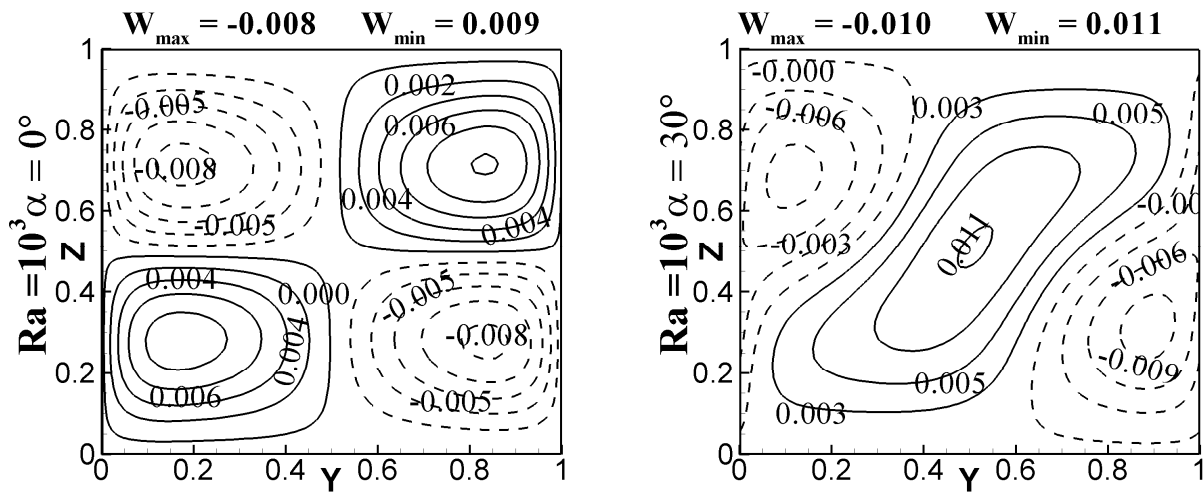


Figure 10. Cont.

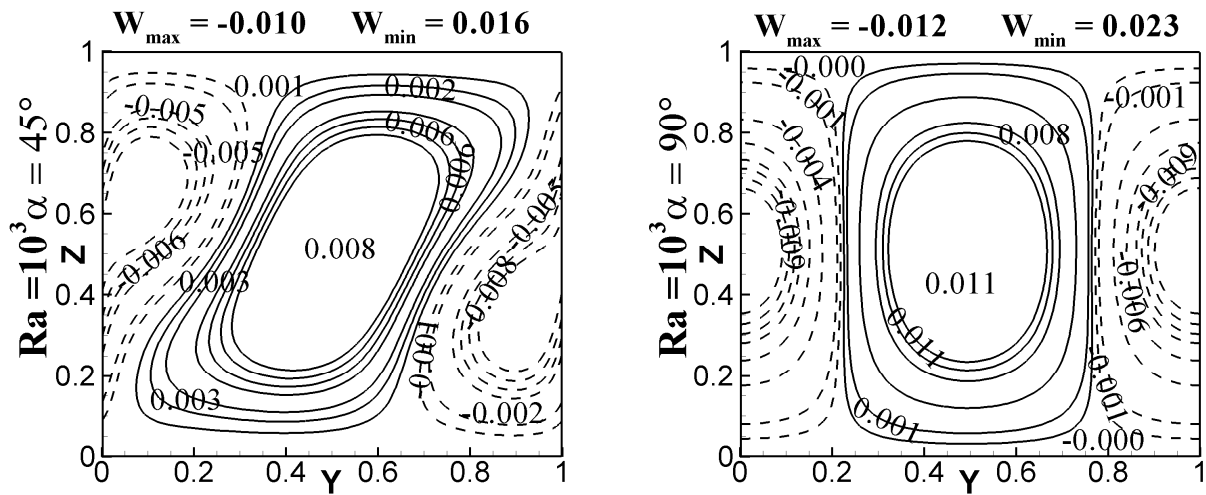


Figure 10. *w*-velocity contours of MWCNT nanoparticles ($\varphi = 0.04$) for different values of inclination angles $\alpha = (0^\circ, 30^\circ, 45^\circ$ and $90^\circ)$ and $Ra = 10^3$ at (y, z) plane.

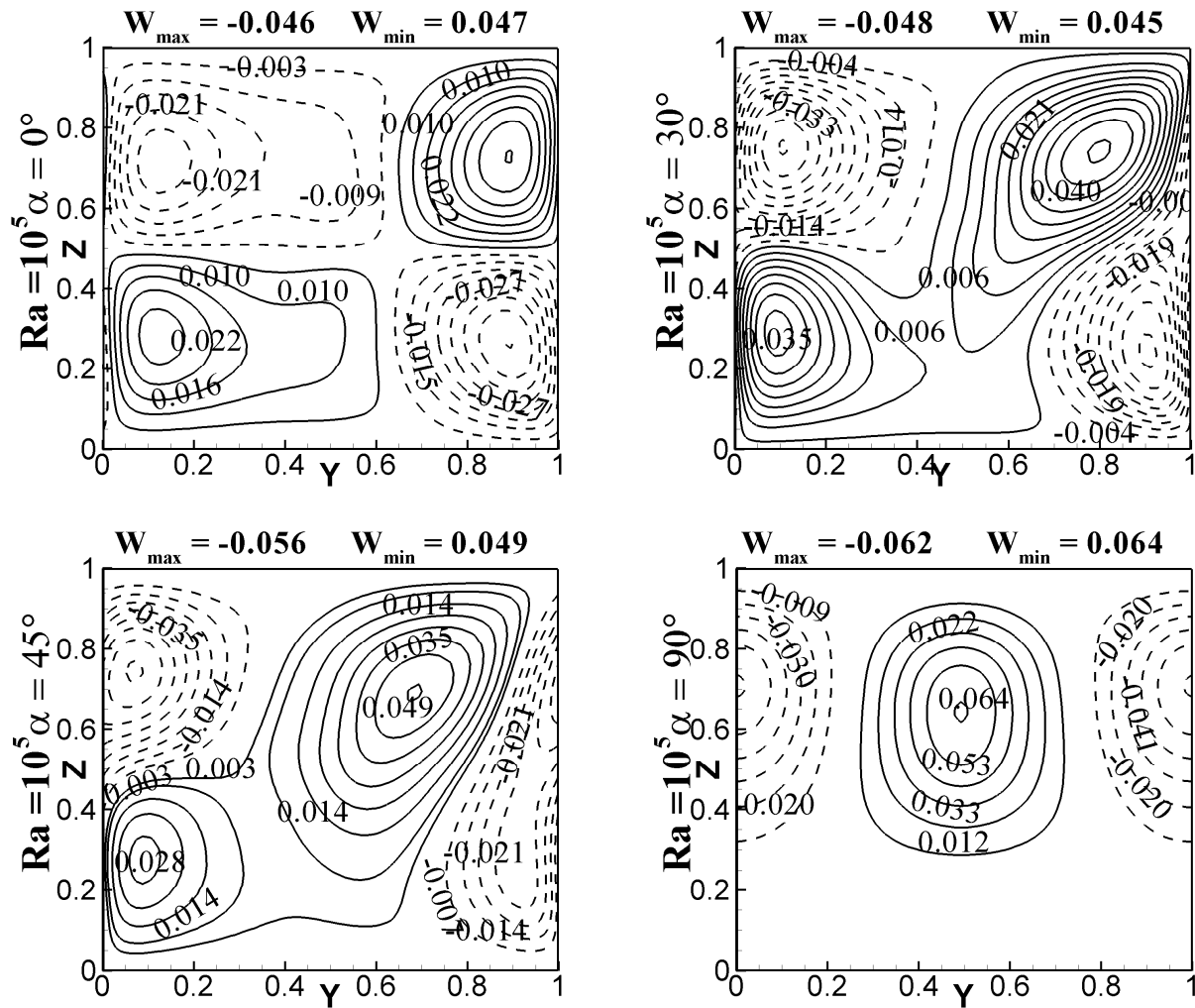


Figure 11. *w*-velocity contours of MWCNT nanoparticles ($\varphi = 0.04$) for different values of inclination angles $\alpha = (0^\circ, 30^\circ, 45^\circ$ and $90^\circ)$ and $Ra = 10^5$ at (y, z) plane.

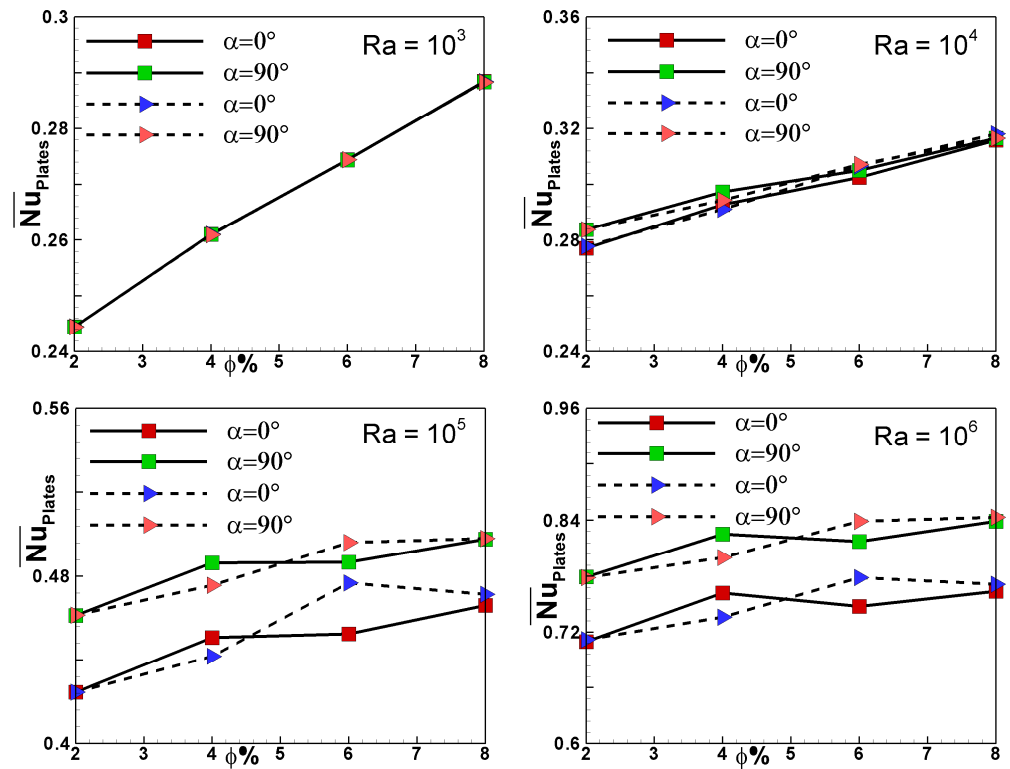


Figure 12. Variation of the average Nusselt number along the plates against the volume fraction for MWCNT (solid lines) and SWCNT (dashed) nanoparticles at the inclination angles $\alpha = 0^\circ$ and $\alpha = 90^\circ$ and ($10^3 \leq Ra \leq 10^6$).

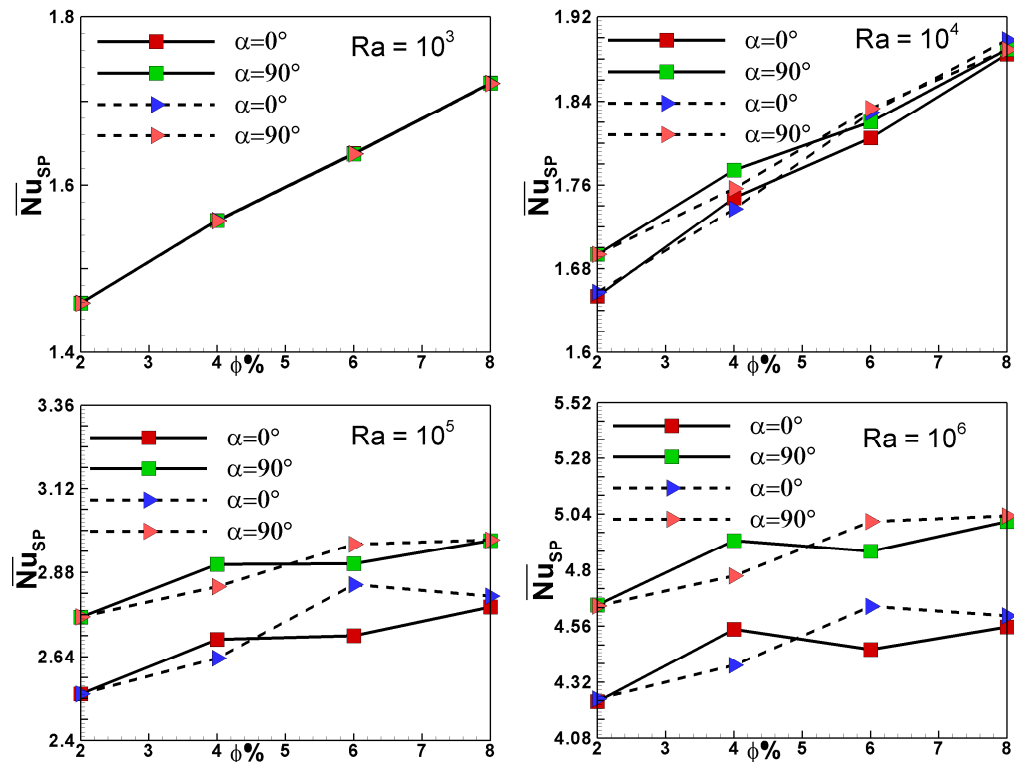


Figure 13. Variation of the average Nusselt number of the inner spheres against the volume fraction for MWCNT (solid lines) and SWCNT (dashed) nanoparticles at the inclination angles $\alpha = 0^\circ$ and $\alpha = 90^\circ$ and ($10^3 \leq Ra \leq 10^6$).

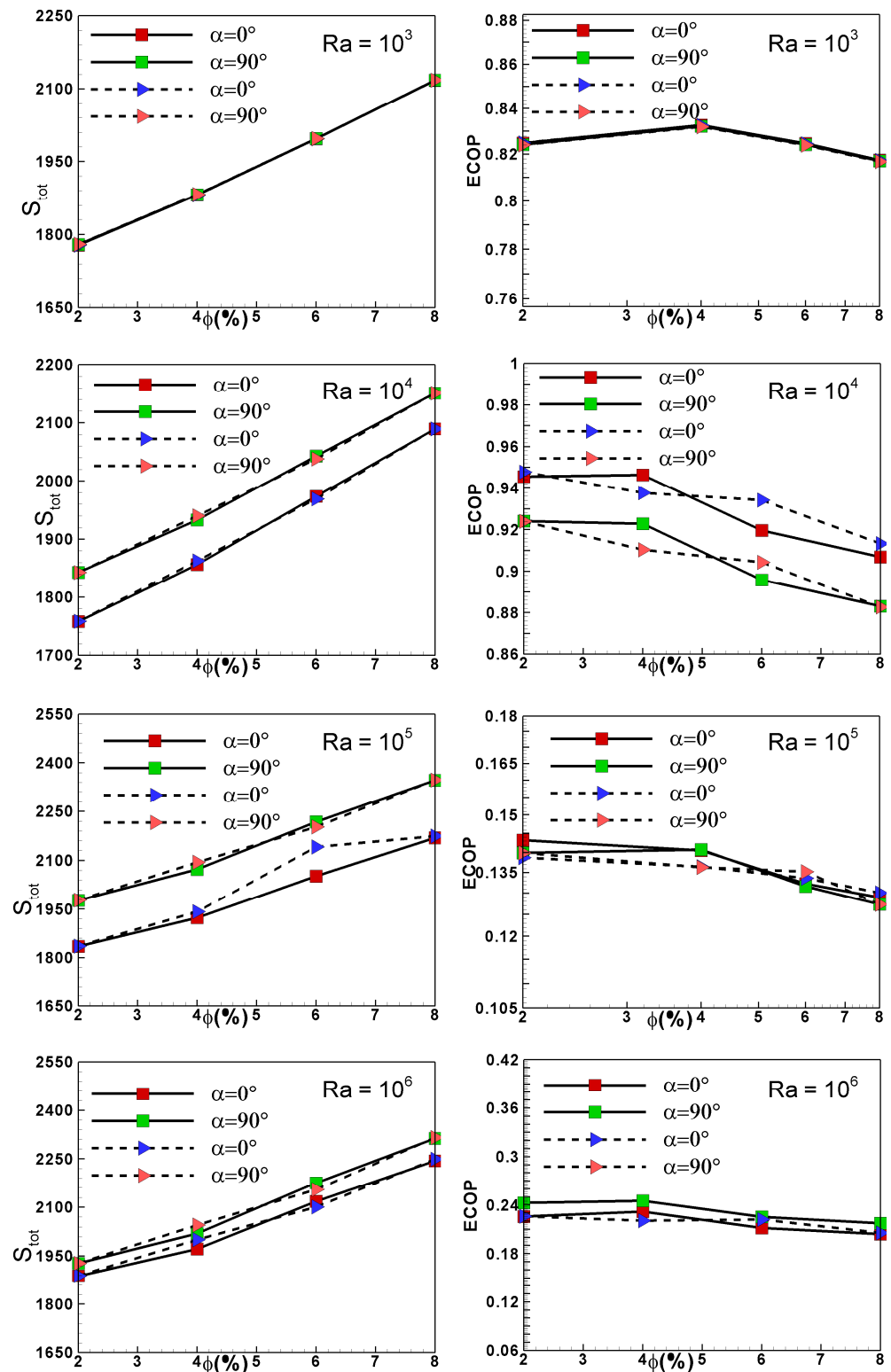


Figure 14. The Profiles of total entropy generation or total irreversibility (left) and ECOP (right) against the volume fractions of MWCNT (solid lines) and SWCNT (dashed) nanoparticles ($\phi = 0.04$) for various Rayleigh numbers and two extreme inclinations $\alpha = 0^\circ$ and 90° .

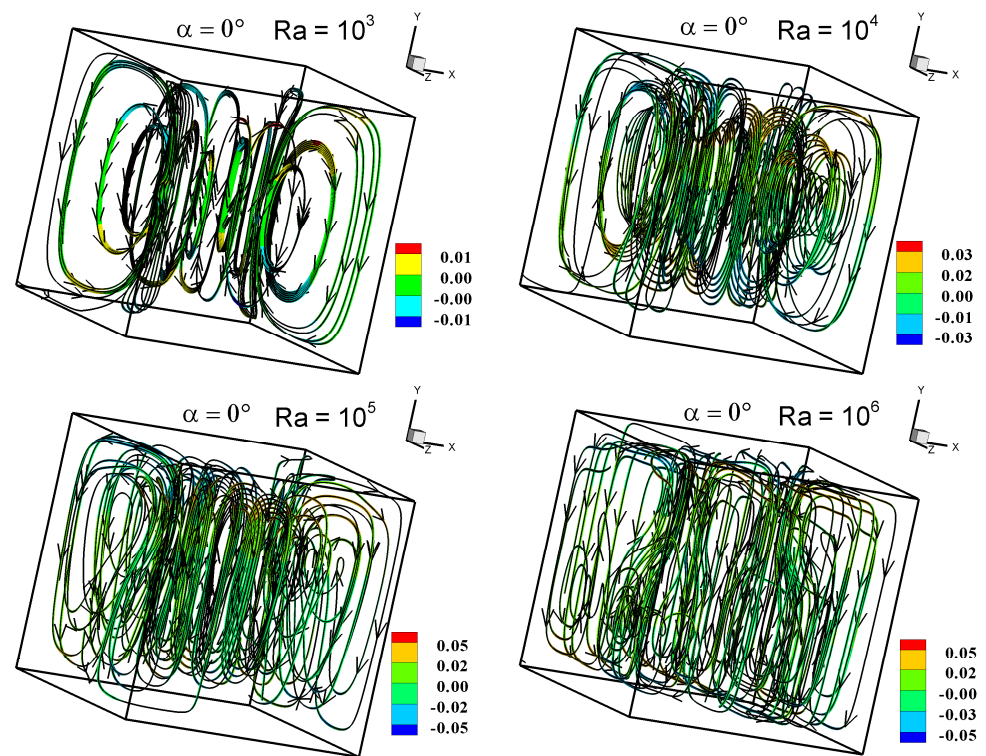


Figure 15. Fluid particle contours of MWCNT nanoparticles ($\phi = 0.04$) for different Ra and $\alpha = 0^\circ$.

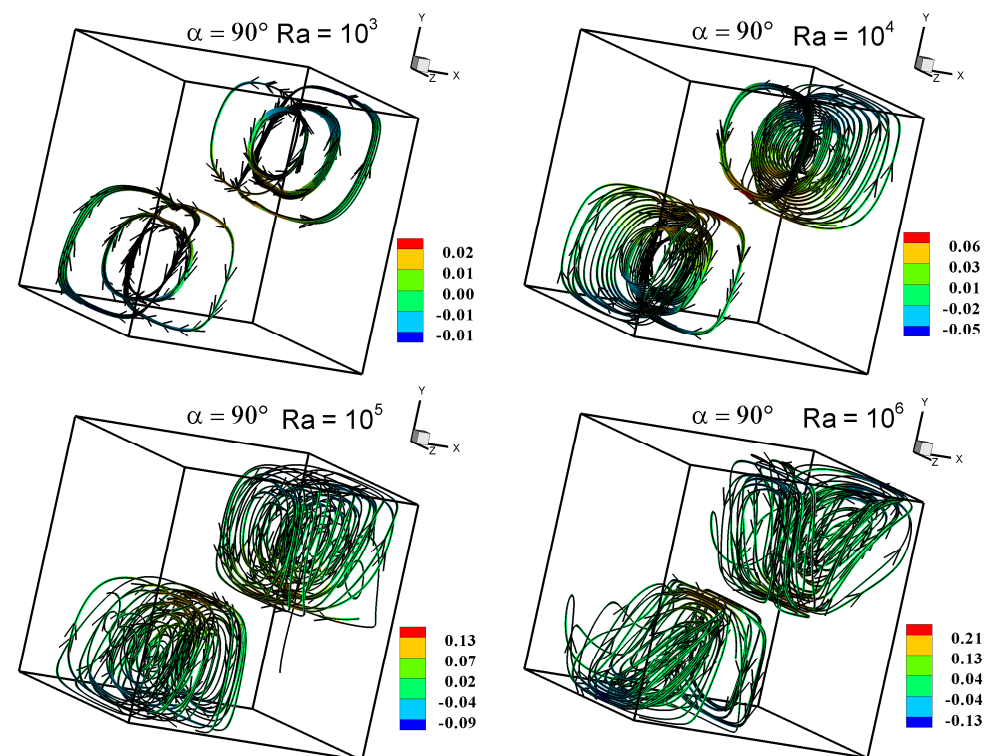


Figure 16. Fluid particle contours of MWCNT nanoparticles ($\phi = 0.04$) for different Ra and $\alpha = 90^\circ$.

Table 4. The average values of heat transfer along the plates for MWCNT nanoparticles at various values of Rayleigh numbers, solid volume fractions and inclination angles.

Ra	\overline{Nu}_{plates}			
	10^3	10^4	10^5	10^6
$\varphi = 2\%$				
0°	0.24450	0.27706	0.38566	0.70967
30°	0.24448	0.27643	0.42194	0.74088
45°	0.24446	0.27737	0.42794	0.74826
60°	0.24449	0.28000	0.44597	0.76289
90°	0.24448	0.28381	0.46125	0.77923
$\varphi = 4\%$				
0°	0.26102	0.29282	0.45068	0.76194
30°	0.26100	0.37914	0.83492	1.91171
45°	0.26098	0.37999	0.83624	1.86822
60°	0.26097	0.38302	0.84721	1.88346
90°	0.24458	0.29731	0.48638	0.82539
$\varphi = 6\%$				
0°	0.27441	0.30244	0.45243	0.74742
30°	0.27438	0.30150	0.44881	0.77642
45°	0.27436	0.30156	0.45106	0.78784
60°	0.27435	0.30276	0.46801	0.804131
90°	0.27434	0.30499	0.48664	0.81751
$\varphi = 8\%$				
0°	0.28849	0.31581	0.46610	0.76365
30°	0.28846	0.31655	0.83914	0.81034
45°	0.28844	0.31627	0.83943	0.82333
60°	0.28843	0.31684	0.48523	0.83943
90°	0.28841	0.31655	0.49773	0.83914

Table 5. The average heat transfer values of the spheres for MWCNT nanoparticles at different Rayleigh numbers, solid volume fractions and inclination angles.

Ra	\overline{Nu}_{sphere}			
	10^3	10^4	10^5	10^6
$\varphi = 2\%$				
0°	1.45926	1.65362	2.51827	4.23556
30°	1.45914	1.64987	2.61822	4.42180
45°	1.45906	1.65544	2.67212	4.46586
60°	1.45909	1.67118	2.68985	4.55316
90°	1.45901	1.69390	2.75288	4.65070

Table 5. *Cont.*

Ra	\overline{Nu}_{sphere}			
	10^3	10^4	10^5	10^6
$\varphi = 4\%$				
0°	1.55789	1.74768	2.68985	4.74750
30°	1.55774	2.26284	2.98310	4.80970
45°	1.55765	2.26793	2.99095	4.90013
60°	1.55757	2.28600	3.05644	4.92110
90°	1.55753	2.29448	3.20291	4.94619
$\varphi = 6\%$				
0°	1.63777	2.30506	3.40030	5.06087
30°	1.63762	2.49946	3.47864	5.23394
45°	1.63751	2.59982	3.52208	5.40209
60°	1.63741	2.60698	3.55327	5.45930
90°	1.63735	2.82032	3.60445	5.47919
$\varphi = 8\%$				
0°	1.72181	2.88486	3.78184	5.55774
30°	1.72166	2.90930	3.88828	5.83641
45°	1.72155	2.92760	3.9002	5.91389
60°	1.72145	2.94105	3.92601	5.94002
90°	1.72137	2.98930	3.97064	5.96828

Table 6. The average heat transfer values along the plates for SWCNT nanoparticles at different Rayleigh numbers, solid volume fractions and inclination angles.

Ra	\overline{Nu}_{plates}			
	10^3	10^4	10^5	10^6
$\varphi = 2\%$				
0°	0.24451	0.27773	0.42447	0.71178
30°	0.24448	0.27691	0.42299	0.74202
45°	0.24446	0.27761	0.42821	0.74945
60°	0.24445	0.28006	0.44585	0.76334
90°	0.24444	0.28378	0.46143	0.77863
$\varphi = 4\%$				
0°	0.26102	0.29109	0.44169	0.73613
30°	0.26098	0.28994	0.43880	0.76453
45°	0.26096	0.28999	0.44143	0.77408
60°	0.26094	0.29152	0.45818	0.78782
90°	0.26092	0.29434	0.47572	0.80004

Table 6. *Cont.*

Ra	\overline{Nu}_{plates}			
	10^3	10^4	10^5	10^6
$\varphi = 6\%$				
0°	0.27439	0.30654	0.47679	0.77833
30°	0.27436	0.30511	0.46149	0.80342
45°	0.27433	0.30461	0.46172	0.81472
60°	0.27430	0.30529	0.47679	0.82740
90°	0.27428	0.30717	0.49610	0.83902
$\varphi = 8\%$				
0°	0.28847	0.31803	0.47132	0.77144
30°	0.28843	0.31639	0.46600	0.79502
45°	0.28840	0.31547	0.46406	0.80775
60°	0.28837	0.31545	0.47702	0.82229
90°	0.28835	0.31646	0.49810	0.84323

Table 7. The average heat transfer values of the spheres for SWCNT nanoparticles at different Rayleigh numbers, solid volume fractions and inclination angles.

Ra	\overline{Nu}_{sphere}			
	10^3	10^4	10^5	10^6
$\varphi = 2\%$				
0°	1.45932	1.65762	2.53337	4.24813
30°	1.45917	1.65268	2.52457	4.42863
45°	1.45906	1.65687	2.55571	4.47298
60°	1.45898	1.67152	2.66098	4.55587
90°	1.45894	1.69370	2.75397	4.64716
$\varphi = 4\%$				
0°	1.55785	1.73736	2.63620	4.39350
30°	1.55766	1.73045	2.61894	4.56298
45°	1.55752	1.73078	2.63459	4.61998
60°	1.55739	1.73989	2.73459	4.70197
90°	1.55730	1.75675	2.83925	4.77491
$\varphi = 6\%$				
0°	1.63770	1.82953	2.84567	4.64534
30°	1.63749	1.82100	2.75434	4.79511
45°	1.63732	1.81802	2.75570	4.86255
60°	1.63716	1.82209	2.84567	4.93822
90°	1.63704	1.83331	2.96091	5.00756

Table 7. Cont.

Ra	\overline{Nu}_{sphere}			
	10^3	10^4	10^5	10^6
$\varphi = 8\%$				
0°	1.72170	1.89815	2.81298	4.60420
30°	1.72148	1.88837	2.78129	4.74492
45°	1.72130	1.88282	2.76966	4.82093
60°	1.72113	1.88270	2.84703	4.90770
90°	1.72099	1.88876	2.97282	5.03268

5. Concluding Remarks

Water-based carbon nanotubes flow field and heat transfer characteristics over two inclined plates induced by two spaced spheres with the entropy generation are analyzed numerically in this paper. The finite volume method is utilized to solve the resulting equations. The effects of Rayleigh number, inclination angle of the plates, nanoparticles type and the volume fraction of nanoparticles on the fluid flow and heat transfer are presented through graphs and tables. The thermal performance of the current physical domain is evaluated through the ecological coefficient of performance (ECOP). Results have clearly indicated that local Nusselt number over the top plate increases with increasing Ra for MWCNT nanoparticles at the angle of tilt $\alpha = 45^\circ$, with an optimal rate equating to 3.2 at $Y = 0.85$ for $Ra = 10^6$. However, the same increases with increasing Rayleigh number for SWCNT nanoparticles at the angle of tilt $\alpha = 45^\circ$, with an optimal rate equating to 1.5 at $Y = 0.85$ for $Ra = 10^6$, which is less than half compared to MWCNT. Furthermore, it is inferred that the average Nusselt number of MWCNT nanoparticles over the plates increases gradually with an Ra of 63.15% from the inclination 0° to 30° . Thereby, the optimal average heat transfer over the plates for MWCNT nanoparticles equates to 1.9 which is obtained for $\alpha = 30^\circ$ and $Ra = 10^6$, whilst, for SWCNT nanoparticles it equates to 0.9 which is obtained for $\alpha = 90^\circ$ and $Ra = 10^6$. Concerning the Bejan numbers for MWCNT nanoparticles, $Be(\alpha = 90^\circ) > Be(\alpha = 0^\circ) > Be(\alpha = 30^\circ)$. However, for SWCNT nanoparticles, $Be(\alpha = 90^\circ) > Be(\alpha = 30^\circ) > Be(\alpha = 0^\circ)$. For both MWCNT and SWCNT nanoparticles, the ECOP decreases from 0.82 for $Ra = 10^3$ to 0.24 for $Ra = 10^6$ (70.73% diminution).

We are going to extend this work soon to the unsteady state case of MHD natural convective heat transfer using the same physical geometry. A study is already underway and will allow us to explore configurations with high Rayleigh numbers.

Author Contributions: Conceptualization, H.A. and B.S.; methodology, B.S. and N.H.; software, B.S.; validation, B.S., M.A.N.; and N.H.; formal analysis, B.S. and M.A.-S.; investigation, B.S., and M.A.N.; resources, H.A. and M.A.-S.; data curation, B.S.; writing—original draft preparation, B.S.; writing—review and editing, N.H., B.S. and M.A.-S.; visualization, H.A., B.S. and N.H.; supervision, B.S.; project administration, B.S.; funding acquisition, H.A. All authors have read and agreed to the published version of the manuscript.

Funding: This work was supported by the Deanship of Scientific Research, Vice Presidency for Graduate Studies and Scientific Research, King Faisal University, Saudi Arabia (Project No. AN00082).

Institutional Review Board Statement: Not applicable.

Informed Consent Statement: Not applicable.

Data Availability Statement: The data that support the findings of this study are available from the corresponding author upon reasonable request.

Acknowledgments: This work was supported through the Annual Funding track by the Deanship of Scientific Research, Vice Presidency for Graduate Studies and Scientific Research, King Faisal University, Saudi Arabia [Project No. AN00082].

Conflicts of Interest: The authors declare no conflict of interest.

Nomenclature

$\langle Be \rangle$	Bejan number
C	specific heat capacity ($Jkg^{-1} K^{-1}$)
p	width of the channel wall (m)
D	gravitational acceleration (ms^{-2})
g	thermal conductivity ($Wm^{-1} K^{-1}$)
k	length of the Plates and distance between upper and lower wall of the plates (m)
\overline{Nu}	Average Nusselt number
n	normal direction
Pr	Prandtl number
P_0	Pressure scale
\vec{q}	Heat flux vector (W/m^2)
Ra	Rayleigh number
T_c	cold wall temperature (K)
T_h	hot wall temperature (K)
T	Temperature (K)
t	dimensionless time
u, v, w	dimensionless velocity components
x, y, z	dimensionless Cartesian coordinates
Ra	Rayleigh number
Greek symbols	
ϕ	solid volume fraction
α	thermal diffusivity (m^2/s)
θ	dimensionless temperature, $\theta = (T - T_c)/(T_h - T_c)$
ν	kinematics viscosity (m^2/s)
μ	dynamic viscosity ($kg/(m.s)$)
ρ	fluid density (kg/m^3)
β	coefficient of thermal expansion (K^{-1})
φ	Irreversibility coefficient
Ω	Global domain
subscripts	
*	Dimensional variable
max	maximum
c	cold
h	hot
Avg	average
TG	thermal gradient
VG	velocity gradient
Loc	local
Tot	total

References

- Hdhiri, N.; Beya, B.B.; Lili, T. Effects of internal heat generation or absorption on heat transfer and fluid flow within partially heated square enclosure: Homogeneous fluids and porous media. *J. Porous Media* **2015**, *18*, 415–435. [\[CrossRef\]](#)
- Hdhiri, N.; Beya, B.B. Internal heat generation/or absorption phenomena in three-dimensional natural convection flow within enclosure filled with different working fluids. *Int. J. Numer. Methods Heat Fluid Flow* **2018**, *28*, 878–908. [\[CrossRef\]](#)
- Awasarmol, U.V.; Pise, A.T. An experimental investigation of natural convection heat transfer enhancement from perforated rectangular fins array at different inclinations. *Exp. Therm Fluid Sci.* **2015**, *68*, 145–154. [\[CrossRef\]](#)
- Solomon, A.B.; Sharifpur, M.; Ottermann, T.; Grobler, C.; Joubert, M.; Meyer, J.P. Natural convection enhancement in a porous cavity with Al_2O_3 -Ethylene glycol/water nanofluids. *Int. J. Heat Mass Transf.* **2017**, *108*, 1324–1334. [\[CrossRef\]](#)
- Choi, S.U.; Eastman, J.A. Enhancing Thermal Conductivity of Fluids with Nanoaprticles. In Proceedings of the ASME International Mechanical Engineering Congress and Exposition, San Francisco, CA, USA, 12–17 November 1995; Volume 66, pp. 99–105, 718–720.
- Javadi, F.S.; Saidur, R.; Kamalisarvestani, M. Investigating performance improvement of solar collectors by using nanofluids, *Renew. Sustain. Energy Rev.* **2013**, *28*, 232–245. [\[CrossRef\]](#)

7. Sokhansefat, T.; Kasaeian, A.B.; Kowsary, F. Heat transfer enhancement in parabolic trough collector tube using Al_2O_3 /synthetic oil nanofluid. *Renew. Sustain. Energy Rev.* **2014**, *33*, 636–644. [[CrossRef](#)]
8. Kumar, V.; Madhukesh, J.K.; Jyothi, A.M.; Prasannakumara, B.C.; Khan, M.I.; Chu, Y.M. Analysis of single and multi-wall carbon nanotubes (SWCNT/MWCNT) in the flow of Maxwell nanofluid with the impact of magnetic dipole. *Comput. Theor. Chem.* **2021**, *1200*, 113223. [[CrossRef](#)]
9. Waqas, H.; Farooq, U.; Naseem, R.; Hussain, S.; Alghamdi, M. Impact of MHD radiative flow of hybrid nanofluid over a rotating disk. *Case Stud. Therm. Eng.* **2021**, *26*, 101015. [[CrossRef](#)]
10. Sheikholeslami, M.; Ellahi, R. Three dimensional mesoscopic simulation of magnetic field effect on natural convection of nanofluid. *Int. J. Heat Mass Transf.* **2015**, *89*, 799–808. [[CrossRef](#)]
11. Sheikholeslami, M.; Shehzad, S.A.; Li, Z. Water based nanofluid free convection heat transfer in a three dimensional porous cavity with hot sphere obstacle in existence of Lorenz forces. *Int. J. Heat Mass Transf.* **2018**, *125*, 375–386. [[CrossRef](#)]
12. Benos, L.T.; Karvelas, E.G.; Sarris, I.E. A theoretical model for the magnetohydrodynamic natural convection of a CNT-water nanofluid incorporating a renovated Hamilton-Crosser model. *Int. J. Heat Mass Transf.* **2019**, *135*, 548–560. [[CrossRef](#)]
13. Ahmed, N.; Khan, U.; Mohyud-Din, S.T. Modified heat transfer flow model for SWCNTs-H₂O and MWCNTs-H₂O over a curved stretchable semi infinite region with thermal jump and velocity slip: A numerical simulation. *Phys. A* **2020**, *545*, 123431. [[CrossRef](#)]
14. Asjad, M.I.; Aleem, M.; Ahmadian, A.; Salahshour, S.; Ferrara, M. New trends of fractional modeling and heat and mass transfer investigation of (SWCNTs and MWCNTs)-CMC based nanofluids flow over inclined plate with generalized boundary conditions. *Chin. J. Phys.* **2020**, *66*, 497–516. [[CrossRef](#)]
15. Gholami, M.; Nazari, M.R.; Talebi, M.H.; Pourfattah, F.; Akbari, O.A.; Toghraie, D. Natural convection heat transfer enhancement of different nanofluids by adding dimple fins on a vertical channel wall. *Chin. J. Chem. Eng.* **2020**, *28*, 643–659. [[CrossRef](#)]
16. Alwawi, F.A.; Alkawasbeh, H.T.; Rashad, A.M.; Idris, R. MHD natural convection of Sodium Alginate Casson nanofluid over a solid sphere. *Results Phys.* **2020**, *16*, 102818. [[CrossRef](#)]
17. Shahsavari, A.; Sardari, P.T.; Toghraie, D. Free convection heat transfer and entropy generation analysis of water-Fe₃O₄/CNT hybrid nanofluid in a concentric annulus. *Int. J. Numer. Methods Heat Fluid Flow* **2019**, *29*, 915–934. [[CrossRef](#)]
18. Shahsavari, A.; Rashidi, M.; Mosghani, M.M.; Toghraie, D.; Talebizadehsardari, P. A numerical investigation on the influence of nanoadditive shape on the natural convection and entropy generation inside a rectangle-shaped finned concentric annulus filled with boehmite alumina nanofluid using two-phase mixture model. *J. Therm. Anal. Calorim.* **2020**, *141*, 915–930. [[CrossRef](#)]
19. Souayeh, B.; Ali Abro, K.; Alfannakh, H.; Al Nuwairan, M.; Yasin, A. Application of Fourier Sine Transform to Carbon Nanotubes Suspended in Ethylene Glycol for the Enhancement of Heat Transfer. *Energies* **2022**, *15*, 1200. [[CrossRef](#)]
20. Al Nuwairan, M.; Souayeh, B. Augmentation of Heat Transfer in a Circular Channel with Inline and Staggered Baffles. *Energies* **2021**, *14*, 8593. [[CrossRef](#)]
21. Mehryan, S.A.M.; Ghalambaz, M.; Gargari, L.S.; Hajjar, A.; Sheremet, M. Natural convection flow of a suspension containing nano-encapsulated phase change particles in an eccentric annulus. *J. Energy Storage* **2020**, *28*, 101236. [[CrossRef](#)]
22. Ghalambaz, M.; Sheremet, M.A.; Mehryan SA, M.; Kashkooli, F.M.; Pop, I. Local thermal non-equilibrium analysis of conjugate free convection within a porous enclosure occupied with Ag-MgO hybrid nanofluid. *J. Therm. Anal. Calorim.* **2019**, *135*, 1381–1398. [[CrossRef](#)]
23. Souayeh, B.; Kumar, K.G.; Reddy, M.G.; Rani, S.; Hdhiri, N.; Alfannakh, H.; Rahimi-Gorji, M. Slip flow and radiative heat transfer behavior of Titanium alloy and ferromagnetic nanoparticles along with suspension of dusty fluid. *J. Mol. Liq.* **2019**, *290*, 111223. [[CrossRef](#)]
24. Alam, M.W.; Abuzir, A.; Souayeh, B.; Yasin, E.; Hdhiri, N.; Hammami, F. Theoretical analysis of carbon nanotubes (SWCNT/MWCNT) over a Wang's stretching sheet under C-C heat flux. *Phys. Scr.* **2020**, *95*, 10. [[CrossRef](#)]
25. Siavashi, M.; Bordbar, V.; Rahnama, P. Heat transfer and entropy generation study of non-Darcy double-diffusive natural convection in inclined porous enclosures with different source configurations. *Appl. Therm. Eng.* **2017**, *110*, 1462–1475. [[CrossRef](#)]
26. Bondareva, N.S.; Sheremet, M.A.; Oztop, H.F.; Abu-Hamdeh, N. Heatline visualization of MHD natural convection in an inclined wavy open porous cavity filled with a nanofluid with a local heater. *Int. J. Heat Mass Transf.* **2016**, *99*, 872–881. [[CrossRef](#)]
27. Sivaraj, C.; Sheremet, M.A. MHD natural convection in an inclined square porous cavity with a heat conducting solid block. *J. Magn. Magn. Mater.* **2017**, *426*, 351–360. [[CrossRef](#)]
28. Souayeh, B.; Ben-Cheikh, N.; Ben-Beya, B. Numerical simulation of three-dimensional natural convection in a cubic enclosure induced by an isothermally-heated circular cylinder at different inclinations. *Int. J. Therm. Sci.* **2016**, *110*, 325–339. [[CrossRef](#)]
29. Yıldız, Ç.; Yıldız, A.E.; Arıcı, M.; Azmi, N.A.; Shahsavari, A. Influence of dome shape on flow structure, natural convection and entropy generation in enclosures at different inclinations: A comparative study. *Int. J. Mech. Sci.* **2021**, *197*, 106321. [[CrossRef](#)]
30. Emami, R.Y.; Siavashi, M.; Moghaddam, G.S. The effect of inclination angle and hot wall configuration on Cu-water nanofluid natural convection inside a porous square cavity. *Adv. Powder Technol.* **2018**, *29*, 519–536. [[CrossRef](#)]
31. Mamourian, M.; Shirvan, K.M.; Pop, I. Sensitivity analysis for MHD effects and inclination angles on natural convection heat transfer and entropy generation of Al_2O_3 -water nanofluid in square cavity by Response Surface Methodology. *Int. Commun. Heat Mass Transf.* **2016**, *79*, 46–57. [[CrossRef](#)]
32. Samadzadeh, A.; Heris, S.Z.; Hashim, I.; Mahian, O. An experimental investigation on natural convection of non-covalently functionalized MWCNTs nanofluids: Effects of aspect ratio and inclination angle. *Int. Commun. Heat Mass Transf.* **2020**, *111*, 104473. [[CrossRef](#)]

33. Al-Sayegh, R. Influence of external magnetic field inclination on three dimensional buoyancy-driven convection in an open trapezoidal cavity filled with CNT-Water nanofluid. *Int. J. Mech. Sci.* **2018**, *148*, 756–765. [[CrossRef](#)]
34. Abu-Nada, E.; Oztop, H.F. Effects of inclination angle on natural convection in enclosures filled with Cu–water nanofluid. *Int. J. Heat Fluid Flow* **2009**, *30*, 669–678. [[CrossRef](#)]
35. Pordanjani, A.H.; Aghakhani, S.; Alnaqi, A.A.; Afrand, M. Effect of alumina nano-powder on the convection and the entropy generation of water inside an inclined square cavity subjected to a magnetic field: Uniform and non-uniform temperature boundary conditions. *Int. J. Mech. Sci.* **2019**, *152*, 99–117. [[CrossRef](#)]
36. Kashyap, D.; Dass, A.K. Effect of boundary conditions on heat transfer and entropy generation during twophase mixed convection hybrid Al_2O_3 -Cu/water nanofluid flow in a cavity. *Int. J. Mech. Sci.* **2019**, *158*, 45–59. [[CrossRef](#)]
37. Bozorg, M.V.; Siavashi, M. Two-phase mixed convection heat transfer and entropy generation analysis of a non-Newtonian nanofluid inside a cavity with internal rotating heater and cooler. *Int. J. Mech. Sci.* **2019**, *151*, 842–857. [[CrossRef](#)]
38. Souayah, B.; Hdhiri, N.; Alam, M.W.; Hammami, F.; Alfannakh, H. Convective heat transfer and entropy generation around a sphere within Cuboidal enclosure. *J. Thermophys. Heat Transfer* **2020**, *34*, 605–625. [[CrossRef](#)]
39. Singh, B.; Dash, S.K. Natural convection heat transfer from a finned sphere. *Int. J. Heat Mass Transfer* **2015**, *81*, 305–324. [[CrossRef](#)]
40. Chen, L.; Lee, J. Effects of inserted sphere on thermal field and heat-transfer characteristics of face-centered-cubic-structured pebble bed. *Appl. Therm. Eng.* **2020**, *172*, 115151. [[CrossRef](#)]
41. Liu, Z.-Y.; Chu, Y.; Liu, J.; Lu, W.-Q. Numerical investigation of the laminar natural convection heat transfer from the equilateral triangular cluster of three horizontal spheres. *Int. J. Heat Mass Transf.* **2019**, *136*, 924–937. [[CrossRef](#)]
42. Bouaziz, M.; Grisenti, M.; Dedies, R.; Zeghmatti, B. Heat and mass transfer correlation for a porous sphere saturated with liquid evaporated in natural convection flow. *Chem. Eng. Process.* **2002**, *41*, 539–549. [[CrossRef](#)]
43. Souayah, B.; Hammami, F.; Hdhiri, N.; Alam, M.W.; Yasin, E.; Abuzir, A. Simulation of natural convective heat transfer and entropy generation of nanoparticles around two spheres in horizontal arrangement. *Alex. Eng. J.* **2021**, *60*, 2583–2605. [[CrossRef](#)]
44. Sudarsana Reddy, P.; Bhuvana Vijaya, R. Heat and mass transfer enhancement of SWCNTs and MWCNTs based Maxwell nanofluid flow over a vertical cone with slip effects. *Powder Technol.* **2020**, *340*, 253–263. [[CrossRef](#)]
45. Patankar, S.V. *Numerical Heat Transfer and Fluid Flow*; McGraw-Hill: New York, NY, USA, 1980.
46. Brown, D.L.; Cortez, R.; Minion, M.L. Accurate projection methods for the incompressible Navier-Stokes equations. *J. Comput. Phys.* **2001**, *168*, 464–499. [[CrossRef](#)]
47. Hayase, T.; Humphrey, J.A.C.; Greif, R. A consistently formulated QUICK scheme for fast and stable convergence using finite-volume iterative calculation procedures. *J. Comput. Phys.* **1992**, *98*, 108–118. [[CrossRef](#)]
48. Chorin, A.J. Numerical methods for solving incompressible viscous flow problems. *J. Comput. Phys* **1967**, *2*, 12–26. [[CrossRef](#)]
49. Ben-Cheikh, N.; Ben-Beya, B.; Lili, T. A multigrid method for solving the Navier–Stokes/Boussinesq equations. *Commun. Numer. Meth. Eng.* **2008**, *24*, 671–681. [[CrossRef](#)]
50. Brandt, A.; Dendy, J.; Ruppel, H. The multi-grid method for semi-implicit hydrodynamic codes. *J. Comput. Phys.* **1980**, *34*, 348–370. [[CrossRef](#)]
51. Barrett, R.; Berry, M.; Chan, T.F.; Demmel, J.; Donato, J.; Dongarra, J.; Eijkhout, V.; Pozo, R.; Romine, C.; Van der Vorst, H. *Templates for the Solution of Linear Systems: Building Blocks for Iterative Methods*; SIAM Press: Philadelphia, PA, USA, 1994.
52. Ben-Cheikh, N.; Ben-Beya, B.; Lili, T. Benchmark solution for time-dependent natural convection flows with an accelerated full-multigrid method. *Numer. Heat Transf. B* **2007**, *52*, 131–151. [[CrossRef](#)]
53. Hammami, F.; Souayah, B.; Ben-Cheikh, N.; Ben-Beya, B. Computational analysis of fluid flow due to a two-sided lid driven cavity with a circular cylinder. *Comput. Fluids* **2017**, *156*, 317–328. [[CrossRef](#)]
54. Hdhiri, N.; Beya, B.B. Numerical study of laminar mixed convection flow in a lid-driven square cavity filled with porous media: Darcy -Brinkman-Forchheimer and Darcy-Brinkman models. *Int. J. Numer. Methods Heat Fluid Flow* **2018**, *28*, 857–877. [[CrossRef](#)]
55. Bezi, S.; Souayah, B.; Ben-Cheikh, N.; Ben-Beya, B. Numerical simulation of entropy generation due to unsteady natural convection in a semi-annular enclosure filled with nanofluid. *Int. J. Heat Mass Transf.* **2018**, *124*, 841–859. [[CrossRef](#)]
56. Souayah, B.; Hammami, F.; Hdhiri, N.; Alfannakh, H. Unsteady state fluid structure of two-sided nonfacing lid-driven cavity induced by a semicircle at different radii sizes and velocity ratios. *Int. J. Mod. Phys. C* **2019**, *30*, 1950060. [[CrossRef](#)]
57. Hammami, F.; Ben-Cheikh, N.; Ben-Beya, B.; Souayah, B. Combined effects of the velocity and the aspect ratios on the bifurcation phenomena in a two-sided lid-driven cavity flow. *Int. J. Numer. Methods Heat Fluid Flow* **2018**, *28*, 943–962. [[CrossRef](#)]
58. Souayah, B. Flow instability of cylinder embedded within two-parallel moving walls of cuboidal cavity at different radii sizes. *Int. J. Mod. Phys. C* **2020**, *31*, 2050063. [[CrossRef](#)]
59. Pak, B.C.; Cho, Y.I. Hydrodynamic and heat transfer study of dispersed fluids with submicron metallic oxide particles. *Exp. Heat Transf. Int. J.* **1998**, *11*, 151–170. [[CrossRef](#)]
60. Xuan, Y.; Roetzel, W. Conceptions for heat transfer correlation of nanofluids. *Int. J. Heat Mass Transf.* **2000**, *43*, 3701–3707. [[CrossRef](#)]
61. Maxwell, J.C. *A Treatise on Electricity and Magnetism*, 2nd ed.; Oxford University Press: Cambridge, UK, 1904.
62. Brinkman, H.C. The viscosity of concentrated suspensions and solutions. *J. Chem. Phys.* **1952**, *20*, 571. [[CrossRef](#)]
63. Khanafer, K.; Vafai, K.; Lightstone, M. Buoyancy-driven heat transfer enhancement in a two-dimensional enclosure utilizing nanofluids. *Heat Mass Transf.* **2003**, *46*, 3639–3653. [[CrossRef](#)]
64. Rosen, M.A. Second-law analysis: Approach and implications. *Int. J. Energy Res.* **1999**, *33*, 415–429. [[CrossRef](#)]

65. Bejan, A. A second-law analysis in heat transfer. *Energy* **1980**, *5*, 721–732. [[CrossRef](#)]
66. Yoon, H.S.; Yu, D.H.; Ha, M.Y.; Park, Y.G. Three-dimensional natural convection in an enclosure with a sphere at different vertical locations. *Int. J. Heat Mass Transf.* **2010**, *53*, 3143–3155. [[CrossRef](#)]
67. Gulberg, Y.; Feldman, Y. On laminar natural convection inside multi-layered spherical shells. *Int. J. Heat Mass Transf.* **2015**, *91*, 908–921. [[CrossRef](#)]